AFRL-AFOSR-JP-TR-2017-0014

Bio-inspired Nano-capillary Self-powered Fluid Transport in Nanocomposite (NBIT III)

Jingming Xu
BROWN UNIVERSITY IN PROVIDENCE IN STATE OF RI AND PROVIDENCE PLANTATIONS

02/22/2017
Final Report

Air Force Research Laboratory
AF Office Of Scientific Research (AFOSR)/ IOA
Arlington, Virginia 22203
Air Force Materiel Command

REPORT DOCUMENTATION PAGE

Form Approved
OMB No. 0704-0188

1. REPORT DATE *(DD-MM-YYYY)*	**2. REPORT TYPE**	**3. DATES COVERED** *(From - To)*
22-02-2017	Final	14 Aug 2013 to 13 Aug 2016

4. TITLE AND SUBTITLE
Bio-inspired Nano-capillary Self-powered Fluid Transport in Nanocomposite (NBIT III)

5a. CONTRACT NUMBER

5b. GRANT NUMBER
FA2386-13-1-4121

5c. PROGRAM ELEMENT NUMBER
61102F

6. AUTHOR(S)
Jingming Xu

5d. PROJECT NUMBER

5e. TASK NUMBER

5f. WORK UNIT NUMBER

7. PERFORMING ORGANIZATION NAME(S) AND ADDRESS(ES)
BROWN UNIVERSITY IN PROVIDENCE IN STATE OF RI AND PROVIDENCE PLANTATIONS
1 PROSPECT STREET
PROVIDENCE, RI 02912-9079 US

8. PERFORMING ORGANIZATION REPORT NUMBER

9. SPONSORING/MONITORING AGENCY NAME(S) AND ADDRESS(ES)
AOARD
UNIT 45002
APO AP 96338-5002

10. SPONSOR/MONITOR'S ACRONYM(S)
AFRL/AFOSR IOA

11. SPONSOR/MONITOR'S REPORT NUMBER(S)
AFRL-AFOSR-JP-TR-2017-0014

12. DISTRIBUTION/AVAILABILITY STATEMENT
A DISTRIBUTION UNLIMITED: PB Public Release

13. SUPPLEMENTARY NOTES

14. ABSTRACT

In this final report, they highlight their attempt to develop a method for generating networks of micro- and nano-capillaries within a ceramic composite during the sintering process at atmospheric pressure. They then present test results of the multifunctional composites for self-powered supply of fluids to the contact (load-bearing) surface via the capillary networks from a fluid reservoir. As a further extension, a self-regulation mechanism is added into the design to enable temperature-controlled self-powered lubrication, and tested in a model system. The method is adaptable to various structural shapes, scalable in size, and applicable to both bio-physiologic and mechanic composite systems.

15. SUBJECT TERMS
NBIT, Nanoscience

16. SECURITY CLASSIFICATION OF:			**17. LIMITATION OF ABSTRACT**	**18. NUMBER OF PAGES**	**19a. NAME OF RESPONSIBLE PERSON**
a. REPORT	**b. ABSTRACT**	**c. THIS PAGE**			SERNA, MARIO
Unclassified	Unclassified	Unclassified	SAR	39	**19b. TELEPHONE NUMBER** *(Include area code)* 315-227-7002

Final Report for AOARD Grant: 13RSZ086 (134121)

"**Bio-inspired nano-capillary self-powered fluid transport in nanocomposite**"

Date: Nov-11-2016

Name of Principal Investigators (PI and Co-PIs):

Ki Tae Nam
- e-mail address : nkitae@snu.ac.kr
- Institution : Seoul National University, Republic of Korea
- Mailing Address : Gwanak-gu, Gwanak-ro 1, Seoul National University, 31 dong 317 ho, Seoul, Republic of Korea
- Phone : 82-2-880-7094
- Fax :

Jimmy Xu
- e-mail address : jimmy_xu@brown.edu
- Institution : Brown University, USA
- Mailing Address : 182 Hope St., Providence, RI 02912, USA
- Phone : 1-401-863-1439
- Fax : 1-401-863-9107

Period of Performance: Aug/19/2013 – Aug/13/2016

Abstract:

Inspired by composite materials in nature, e.g. bone, with both sufficient mechanical strength and permeability, we designed and fabricated hierarchically organized channels with tapered cross-sections inside a bioceramic. A novel pressurized sintering process was developed to enable the fabrication. The tapering of the cross-sections of the channels was along the channel length and controlled by a pressure gradient during sintering. The resultant composite showed a mechanical strength of the bioceramics with nano-channels built-in similar to that of human bone and an ability to self-power the transport of fluids and nutrients. Notably, by tracing transport of radioactive fludeoxyglucose (^{18}F-FDG), we directly demonstrated sustained cellular growth by self-powered uptake of nutrient via the nano-channels, replicating the expected function of nano-channels in natural system. This design and process can be adapted to a multitude of different composite materials to enhance both their permeability and strength for industrial applications.

An additional functionality realized was self-lubrication. It is known that ceramics with a modulus of elasticity higher than that of high carbon chrome bearing steel, ceramic axes and ball-bearing turbos exhibit less deformation at contact points and therefore a greater stress under the same load. Combined with a lower thermal conductivity, their working temperature increases and their load capacity decreases more rapidly in operation. In nature, however, a ceramic composite system, bone, is known for its superior load-bearing capacity, and its self-protection at the high-stress moving-contact points (joints). Less known but no less important is the fact that it does so with self-lubrication, through a built-in capillary networks for self-powered supply of lubricants and coolants, as well as nutrient and growth factor. This is another example from Nature that inspired our efforts and led to designs and demonstrations of multifunctional ceramic composites capable of self-powered supplies of fluidics while retaining and even enhancing the mechanical load-bearing capability for engineering applications.

In this annual report, we highlight our attempt to develop a method for generating networks of micro- and nano-capillaries within a ceramic composite during the sintering process at atmospheric pressure. We then present test results of the multifunctional composites for self-powered supply of fluids to the contact (load-bearing) surface via the capillary networks from a fluid reservoir. As a further extension, a self-regulation mechanism is added into the design to enable temperature-controlled self-powered lubrication, and tested in a model system. The method is adaptable to various structural shapes, scalable in size, and applicable to both bio-physiologic and mechanic composite systems.

Approach:

Permeability and mechanical strength are both essential for bone materials to enable optimized growth and recovery. Bone implants with efficient permeability can provide nutrients to induce fast tissue regeneration. On the other hand, bone implant material should also have sufficient mechanical strength to support body weight, motion, and mechanical impact. However, until now, permeability and mechanical strength were considered as in conflict for engineering micrometer-scale porous materials. To overcome this problem, we designed and fabricated nano-channel built-in ceramic structure to pursue permeability while retaining, and even enhancing, the desired mechanical strength.

For validation, we tested the capillarity of various designs of ceramic composites with nano-channel built-in, and observed nutrient delivery in a fabricated ceramic composite sample *in situ*, by utilizing Positron Emission Tomography-Computed Tomography (PET-CT). Also, fluid transport tests were conducted quantitatively among various designs of nano-channel structure. Moreover, we confirmed the functionality of sustaining cellular activities at the end facet of the ceramic sample enabled by the nano-channels' self-powered nutrient delivery. The proliferation level and bone mineralization related activity of human bone cells were evaluated. Interestingly, by adding radioactive fludeoxyglucose (^{18}F-FDG) in the fluid at the reservoir end of the nano-channels, we directly demonstrated that actual cellular uptake of ^{18}F-FDG was happening in real time. These results provided the first and conclusive proof that small organisms can proliferate solely by the self-powered supply of nutrients via the nano-channels. One can further expect that the self-powered nano-channel delivery can find applications in other engineering fields, such as ionic charge transport (e.g. distributed battery), heat pipe for efficient cooling, and desalination device with enhanced evaporation/condensation process.

Cross-disciplinary Pursuit and Significance:

In man-made systems, ceramic load-bearing composites have enabled functional devices, e.g. rotors and valves, to operate in high-temperature, light-weight, and corrosion-resistant applications. However, unlike bones, they are designed and structured so far mainly for load-bearing in these mechanical applications.

Separately, there have been biomedical engineering pursuits for composite materials, e.g. synthetic hydroxyapatite (HAP), for bio-physicochemical in vitro and in vivo applications, such as middle ear implants, reconstructive joint replacement, and bone implants etc.). [1-4].

It seems only natural for the developments in the two fields to cross paths and benefit from each other's advances. All the key elements – the concept, theory, design, and base materials are in place and can be co-developed for the interests in developing next generation functional composites for both bio-physiologic and mechanical applications.

The project enabled such experimental tests of the concept, theory, and design of self-powered fluid transport in a composite material as a model platform that mimics the bone in functionality, with fluids and nutrients constantly supplied through micro- and nano-porous networks by capillary forces and/or osmosis [1]. And, like the bone, the primary structural material of body, these porous composites manifest a superior load-bearing capability but can be greater in load-bearing capacity and yet also is cable of self-powered and self-regulated cooling, lubrication, even elf-sustained growth and healing.

For this project, we primarily experimented with the hydroxyapatite [HAP: $Ca_{10}(PO_4)_6(OH)_2$] for structuring the model platform. We performed a number of tests, guided largely by requirements for bone implants. The findings are however generally applicable to other ceramic composites and to engineering applications.

HAP, as a most stable calcium phosphate salt at pH between 4 and 12, have been used in catalysis, fertilizers and pharmaceutical, protein chromatography, water treatment processes, and preparation of biocompatible materials. It is the main inorganic component in calcified hard tissues (e.g., bone and teeth) of vertebrates [5, 6]. Pathologically as a result of functional irregularities, it also can form cartilage arthritis, renal, bladder, and bile stones, atheromatic plaque, and calcification of transplanted cardiac valves [7]. As such, HAP has been employed as a model compound to study bio-mineralization phenomena [8-12].

In many ways, targeting bone implant functions in this project represents a greater challenge. That is because bone implant should satisfy a larger set and often more stringent requirements than ceramic parts in conventional rotors and valves. In addition, the implant should be biocompatible, bioactive, or biodegradable [13]. The implant should have a porous three-dimensional architecture capable of supporting cell and tissue infiltration, transport of nutrients, and development of capillaries [14]. It must have the requisite mechanical properties for supporting loads experienced by the bone to be replaced [15]. Considerable improvements in bone implants are necessary to meet these stringent requirements, particularly for applications in the repair of load-bearing bone, one of which would be in self-lubrication and healing.

Like the moving parts in a ceramic rotor or valve, bone joints are lubricated. They, a marvel of bio-engineering, are structured to maintain their lubrication with lubricin – a

principal boundary lubricating and anti-adhesion protein found in a thick colorless liquid that surrounds joints (synovial fluid). These fluids are self-supplied over the parts of the joint not reached by blood vessels that transport nutrition and lubrication, allowing the bones to glide over each other. However this self-lubrication mechanism could be disrupted, damaged, or simply absent, for example in cases of arthritis or the use of today's implants.

Nevertheless, bone grafts are necessary in orthopaedic surgery for filling bone cavities, treatment of nonunion and replacement of bone lost during trauma and tumor removal. Incorporating fluidic, nutrient, and lubricant supply and management into bone implants would represent a significant step forward in bone implant material development. One outcome of this project is that we have made inroads with our HAP composites by structuring within them distributed networks of gradient capillaries, resembling that found in natural bone [16-18], and conducted a series of experiments and tests to show that it is possible to achieve self-powered supply of nutrients in HAP composite structures.

In the following, we report on details of the advances we made in building capillary networks within an HAP composite and in enabling continuous and spatially distributed supply of lubricants through load-bearing structures, and the findings as a model platform for future extension to ceramic engine.

As a starting point, the HAP composites were formed from a homogeneous mixture of HAP powders and polymers (e.g. PEG or agarose gel). The distributed networks of capillaries in the composite were produced during the sintering process by taking advantage of the phase-separation between the HAP and polymers as well as the pressure-dependent liquid to vapor phase transition. For implant applications, the polymers (e.g. PEG) can be chosen from those that are biocompatible and molecular weight (size) scalable. With this method, high porosity and networked capillaries that are density-variable and size-variable by pressure can be controllably produced in the composite.

In year-3, a further innovation was introduced in the process by which a linear or radial gradient of the porosity and pore size can be obtained. It was accomplished by stacking HAP-agarose gel composites of gradually changing weight percentage of the agarose gel.

The following describes the collaborative efforts between the two teams and the facile synthesis of HAP composite structures of various shapes, all with built-in capillary networks, and the temperature-controlled self-regulation and self-powered supply of lubricants via these networks.

Korean Side: led by Seoul National University, aided in conceptualization, design, and theory from the Brown team

Experiment:

1) Preparation

Hydroxyapatite (HAP: $Ca_{10}(PO_4)_6(OH)_2$) was synthesized by a precipitation method with calcium hydroxide ($Ca(OH)_2$, 99.0%, High Purity Chemical, Japan) and phosphoric acid (H_3PO_4, 85.0%, Junsei Chemical Co., Ltd) in an aqueous base. In distilled water, 0.5 M $Ca(OH)_2$ solution was prepared. After stirring vigorously with a mechanical stirrer (overhead stirrer, MSM-1 Jeio Tech) for an hour, 0.5 M H_3PO_4 was added drop-by-drop using a digital burette (Metrohm 876, Dosimat Plus). The final composition ratio of $Ca(OH)_2$ and H_3PO_4 was 10:6, and the precipitates were aged for 24 hours while stirring at room temperature. The HAP solution was filter-pressed and freeze-dried. Dried HAP powder was mixed with polyethylene glycol (PEG: $HO\text{-}CH_2\text{-}(CH_2\text{-}O\text{-}CH_2\text{-})_n\text{-}CH_2\text{-}OH$) with molecular weights of MW 400 (M = 380-420 g $mole^{-1}$, Sigma Aldrich), MW 2,000 (M = 1800 g $mole^{-1}$, Merck), MW 10000 (M = 9000 g $mole^{-1}$, Merck) and MW 600000 (M = 600000 g $mole^{-1}$, Sigma Aldrich). Weight ratio of HAP and PEG was 10:1 in standard mixture. PEG was dissolved in distilled water and mixed until homogeneous with HAP by grinding.

2) **Fabrication of AMCD-HAP pellet**

To make AMCD-HAP pellets of selected defined porosity, various ratios of HAP-PEG mixture (PEG:HAP = 1:1, 1:5, 1:10) were made into pellets in a 37 mm × 7 mm × 2 mm aspect shape, using a pressure mold, by applying 2 tons of pressure for 3 seconds. The HAP-PEG pellets were sintered at 1,100 °C for 2 hours. During sintering of the AMCD-HAP pellet, a 911.1 g mass right-triangular prism-shaped metal wedge, made from stainless steel (SUS310S) or super alloy (HAYNES230), was placed atop the HAP-PEG pellet to provide a pressure gradient that reflected the shape and mass of the wedge. An alumina ceramic (Al_2O_3) plate was placed between the metal weight and the HAP-PEG pellet to prevent contamination.

3) Fabrication of nonporous HAP pellet and homogeneously porous HAP pellet

To make nonporous HAP pellets, the PEG binder at 0.0001% by weight, was

mixed with HAP powder. To regulate the porosity of the homogeneously porous HAP pellet, the initial ratio between PEG and HAP was controlled by mixing HAP and PEG at a ratio of: 2.55:1, 2.63:1, 3.25:1, 4.95:1 and 10:1. The HAP-PEG mixtures were made into pellets in a 37 mm × 7 mm × 2 mm aspect shape, using a pressure mold, by applying 2 tons of pressure for 3 seconds and sintered at 1,100 °C and 1,300 °C for 2 hours to make homogeneously porous HAP pellet and nonporous HAP pellet, respectively. The porosities of nonporous HAP pellets and homogeneously porous HAP pellets (HAP:PEG = 2.55:1, 2.63:1, 3.25:1, 4.95:1 and 10:1) were $0.19 \pm 0.07\%$ (n = 4), $10.92 \pm 2.00\%$ (n = 6), $7.09 \pm 0.27\%$ (n = 4), $3.02 \pm 0.29\%$ (n = 4), $1.40 \pm 0.16\%$ (n = 4) and $0.78 \pm 0.08\%$ (n = 5), respectively.

4) Characterization and analysis

The surface morphology of the AMCD-HAP was observed by field emission scanning electron microscope (JSM-6330F, JEOL). The images of stained osteoblast cells were obtained using fluorescence microscopy (Axio Observer Inverted Microscope, Carl Zeiss).

5) Porosity analysis

The AMCD-HAP sample was divided into three regions corresponding to variation in the pressure gradient (pressure region 0 ~ 4, 4 ~ 8 and 8 ~ 12, See Figure 4a) to provide the corresponding regions of varied porosity. Gas adsorption-desorption was measured in each of the three regions. N_2 adsorption was measured at 77 K on a BELSORP-mini II (BEL Japan Inc., Japan) after degassing under vacuum at 150 °C for 24 hours. Specific surface area was estimated using the BET (Brunauer-Emmett-Teller) equation with a 0.01 ~ 0.20 relative pressure range. The porosity of each region of AMCD-HAP was calculated by Archimedes' principle, represented as ((immersed mass-dried mass) × (immersed mass-suspended mass)$^{-1}$ × 100%) by using an electronic scale (GR-200, AND) equipped to measure specific gravity (AD-1653, AND).

The distributions of low-density pixels in each region of the AMCD-HAP sample were analyzed by Micro-CT (ZEISS Xradia 510 Versa), according to the porosity measured by Archimedes' principle. The connectivity among the low-density pixels in each region was analyzed using the Amira software.

6) ^{18}F-fluoro-deoxyglucose positron emission tomography (FDG-PET)

To compare fluid migration *in situ* for AMCD-HAP and non-porous HAP pellets, ^{18}F-fluoro-deoxyglucose (FDG) positron emission tomographic (PET) and computed tomography (CT) scanning were performed (NanoPET/CT, Mediso, Medical Imaging Systems, Budapest, Hungary). Each pellet was oriented vertically in a sterile container filled with 3 ml of distilled water containing ^{18}F-FDG (100 *u*Ci). The PET image was acquired by scanning in list mode for 60 minutes and the images were reconstructed. CT and PET images were acquired and reconstructed as maximal intensity projection images. Images were compared using the same image window settings for all images.

7) Capillary rise test

The capillary rise test was performed in a double walled vessel to control temperature. Cooled isopropanol was circulated between the double walls of the vessel to maintain the inside container at a constant temperature of 25 °C. To fix the humidity level at a constant value, the bottom of the inside container was covered with silica gel blue (DaeJung) and Drierite (Hammond Company). AMCD-HAP, non-porous HAP, and homogeneously porous HAP pellets were partially immersed vertically in distilled water. A 1 mm calibrated scale was used to measure the rise of fluid using a red ink dye. The number of samples used for each conditions was n = 3.

8) Cell culture and staining

To observe the growth of human osteoblasts on HAP surfaces exposed to air, blocks of HAP were prepared as described. AMCD-HAP pellets were compared with nonporous HAP pellets as controls. After sintering, the HAP pellets were washed with acetone and distilled water, sterilized at 130 °C for 20 minutes and dried under UV irradiation. A sterilized pellet was placed upright in a plastic tube, forming a reservoir for the osteoblast basal medium (Lonza Clonetics) containing fetal bovine serum (FBS), ascorbic acid and GA-1000. Human osteoblasts (Lonza Clonetics) were seeded on the top surface, which measured 7 mm $\times$ 2 mm, at a density of 1 $\times$ 10^5 cells ml^{-1}. The sample was placed in a water-jacketed incubator maintained at 37 °C in ambient atmosphere supplemented with 5% CO_2. After cell attachment, the medium was partially removed to a level approximately 1 cm below the top surface of the HAP pellet. After 7 days of culture, the pellet was fixed for 10 minutes with 3.7%

formaldehyde diluted in PBS (Cellgro, Mediatech Inc.). The cells were permeabilized with 0.2% Triton X-100 diluted in PBS for 10 minutes. The actin cytoskeleton network was stained with phalloidin (Phalloidin, fluorescein isothiocyanate labeled, Sigma) for 1 hour and nuclei were stained with DAPI (4′,6-Diamidino-2-phenylindole dihydrochloride, Sigma) for 5 minutes. The AMCD-HAP pellet was mounted with Fluoromount (Aqueous Mounting Medium, Sigma) and observed by fluorescence microscopy with appropriate excitation and barrier filters.

9) Cell proliferation and cellular uptake of ^{18}F-FDG

Cells were maintained on the top surface of AMCD-HAP as described for 1 day with the media exchanged for a low glucose formulation (Dulbecco's Modified Eagle's Medium with 1.0 g L^{-1} Glucose, without L-Glutamine, FBS, 10% v v^{-1}, Penicillin 10,000 units ml^{-1}, Streptomycin 10 mg ml^{-1}) to starve cells for glucose. Likewise, low-glucose media was carefully provided to the reservoir to a level approximately 1 cm below the surface of the AMCD-HAP on which the cells grew. After 1 day, low-glucose media was changed with ^{18}F-FDG (0.5 *u*Ci $sample^{-1}$) in PBS, to the same height level. After 1 hour, the AMCD-HAP sample was recovered and its surfaces, except the top surface supporting the cells, were carefully wiped with tissue paper. The AMCD-HAP sample, except the surface supporting the osteoblasts, was washed several times with phosphate buffered saline (PBS) to remove ^{18}F-FDG not incorporated into the osteoblast cells. Cells were released from the AMCD-HAP sample using 3 ml of trypsin-EDTA solution for 3 minutes and the cells recovered. The trypsin-EDTA was neutralized with 7 ml of media and the cells were collected by brief centrifugation at 3000 rpm for 3 minutes and the wash solution discarded. Using a cell counter (ADAM-MC, nanoEntek) and a gamma detector (Wallac 1480 Wizard 3 gamma counter, Turku, Finland), the total cell number was quantified and the radioactive counts per minute (CPM) incorporated into the cells was measured, respectively. For the control sample, exactly the same experimental protocol was conducted only with a nonporous HAP samples with cell number and radioactive incorporation determined compared with that from the AMCD-HAP.

10) Real time PCR

Real time PCR was performed with Rotor gene Q (Qiagen, Santa Clarita, CA) with the Rotor gene SYBR green PCR kit. RNA was extracted from cells using a

RNA extraction reagent (RNAiso Plus, Takara), and first strand cDNA was synthesized by using a QuantiTect reverse transcription kit (Qiagen) with random hexamer primers. The initial activation step for PCR was 3 minutes at 95 °C. Denaturation and combined annealing/extension cycles proceeded at 95 °C for 3 seconds and 60 °C for 10 seconds, respectively. Each sample was subjected to analysis in triplicate. The numbers of samples used for AMCD-HAP and for the control nonporous HAP were both n = 7. The relative quantities of amplified cDNAs were calculated using the ΔC_T method with ribosomal RNA used as the baseline. Primers used for PCR were purchased from QuantiTect Primer Assay (Qiagen): 18S ribosomal RNA (*RRN18S*, QT00199367), secreted protein acidic cysteine-rich (*SPARC*, QT00018620), bone gamma-carboxyglutamate (Gla) protein (*BGLAP*, QT00232771), bone morphogenetic protein 2 (*BMP2*, QT00012544), secreted phosphoprotein 1 (*SPP1*, QT01008798), collagen type I (*COL1*, QT00037793), Runt-related transcription factor 2 (*RUNX2*, QT00020517), and integrin-binding sialoprotein (*BSP*, QT00093709).

Theoretical Approach:

Trees and the vessels in human body are representative examples of natural circulation system. According to 'Allometric scaling law', the metabolic rate is exponentially proportional to the mass of organisms with 3/4 order, and a structural advantage causes the metabolic rate enhancement. In unicellular organisms, they have one-dimensional and primary circulation structure. However, more complex organisms possess center channel like artery and vein which take a main role of transportation, and secondary channels from the center channel like capillaries. This hierarchical structure is designed to connect center and terminal parts of organisms efficiently.

Meanwhile, in the case of tress over 100 meters height, the radius of vessels decreases in nanometer scale, which causes enhancement of capillary effect, according to equation 1. As a result, the permeability of the lower part and the driving force of the capillary effect become maximized, that enable to transport nutriments from the roots to upper part of the tree. The advantage of this structure is displayed in figure 1, by comparing a cylindrical glass tube with conical one, immersed in the water solution. As shown in figure 1b, the radius of each system can be expressed in equation 2. The equilibrium height of risen water is determined by the force equilibrium of surface tension and gravity force. As a result, the height of water

in cylindrical tube and conical tube can be obtained from equation 3 and 4. Figure 1c exhibit theoretical calculation of risen water height in each system. It can be clearly verified that the position of water in conical tube is expected higher than that in cylindrical tube (figure 1c.). Moreover, as angle α increases, this effect is being maximized (figure 1d.) which is in accordance with previous studies. Based on these theoretical understandings, we tried to realize maximized capillary phenomena in our designed ceramic structure, for the first time.

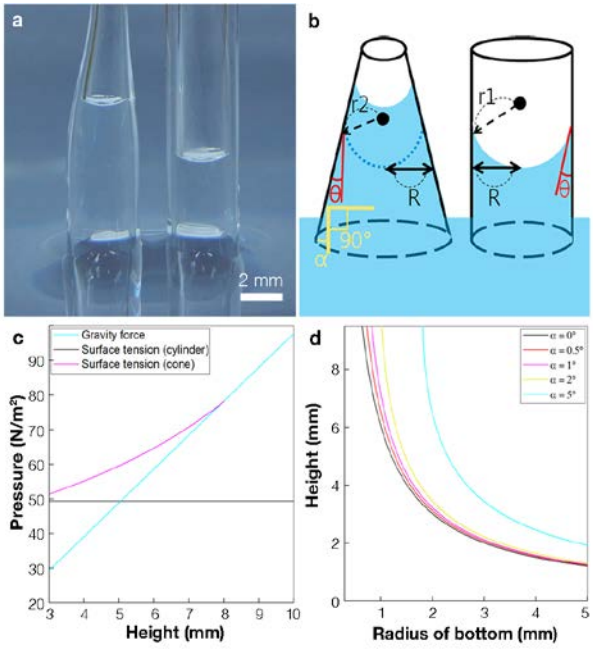

Figure 1. Bio-inspired capillary fluid transport in diameter-tapered channels: a) A “conical tube” and a “cylindrical tube” were both placed upright in pure water. b) Schematic figure of “conical tube” and “cylindrical tube”. c) The theoretical capillary heights of the “conical tube” and “cylindrical tube” are compared by the intersection of surface tension and the force of gravity. d) Capillary heights from tubes with different gradient angle α are compared in calculation.

$$h = \frac{2\gamma\cos\theta}{\rho g r} \quad \text{..... Equation 1.}$$

$$R = r_1\cos\theta = r_2\cos(\theta-\alpha), r_2 = r_1\frac{\cos\theta}{\cos(\theta-\alpha)} \quad \text{..... Equation 2.}$$

$$\rho g h = \frac{2\gamma^{LV}}{r} = \frac{2\gamma^{LV}}{R}\cos\theta \quad \text{..... Equation 3.}$$

$$\frac{2\gamma^{LV}}{r_2} = \frac{2\gamma^{LV}\cos(\theta-\alpha)}{r_1\cos\theta} = \frac{2\gamma^{LV}\cos(\theta-\alpha)}{R} \quad \text{..... Equation 4.}$$

Results and Discussion:

To build nano-channel structure in ceramic by novel pressurized-sintering concept, we created a pressure gradient on the PEG-HAP sample to induce phase separation between polymer and ceramic nanoparticles (Figure 2). We labeled the pressure level along the long-axis of a PEG-HAP pellet, during sintering, from 0 to 12, corresponding to the pressure gradient exerted on the pellet. By theoretical calculation, the greatest local pressure we applied to the PEG-HAP sample was 34.47 KPa, achieved near the heavier end of the metal wedge with the loading gradually decreasing along the length of the wedge.

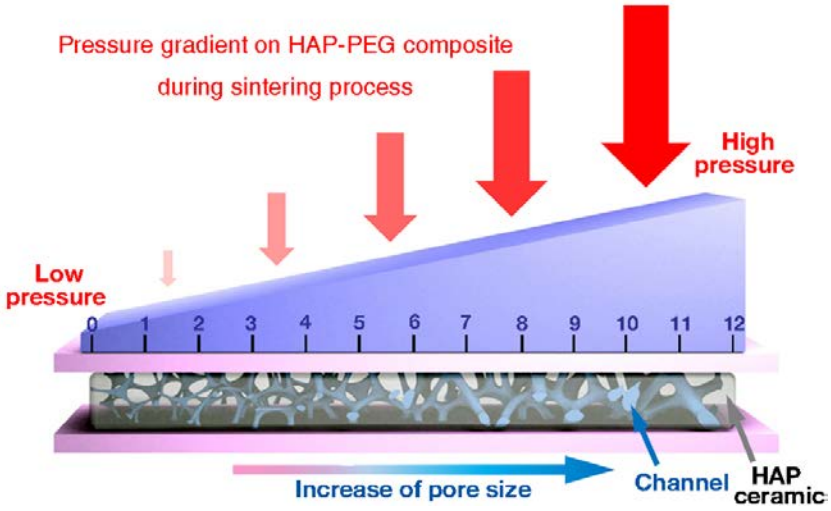

Figure 2. A simple design for creating gradient pressure during sintering process and schematic representation of Aligned Multiple Capillary networks with gradually decreasing Diameter-HAP (AMCD-HAP) showing different porosity sections that correspond to different regions in the pressure gradient. Pressure levels (P level) were labeled from 0 to 12, corresponding to the pressure gradient exerted on an AMCD-HAP during sintering. As the pressure level increases during sintering process, the diameter of the channel (blue) in HAP ceramic (white) increases.

Figure 3a shows stress deformation of nano-channel structure when normal stress and shear stress are applied. When stress was applied in compressive direction, stress was concentrated in both side of the pore, and cause deformation. In the shear stress case, deformation resistance of nano-channels structure was bigger than normal stress case. We demonstrated pore geometry on structural stability using theoretical modeling (Figure 3b). For the same porosity, smaller pore structures more stable which have been largely ignored in other studies on flow through deformable tubes.

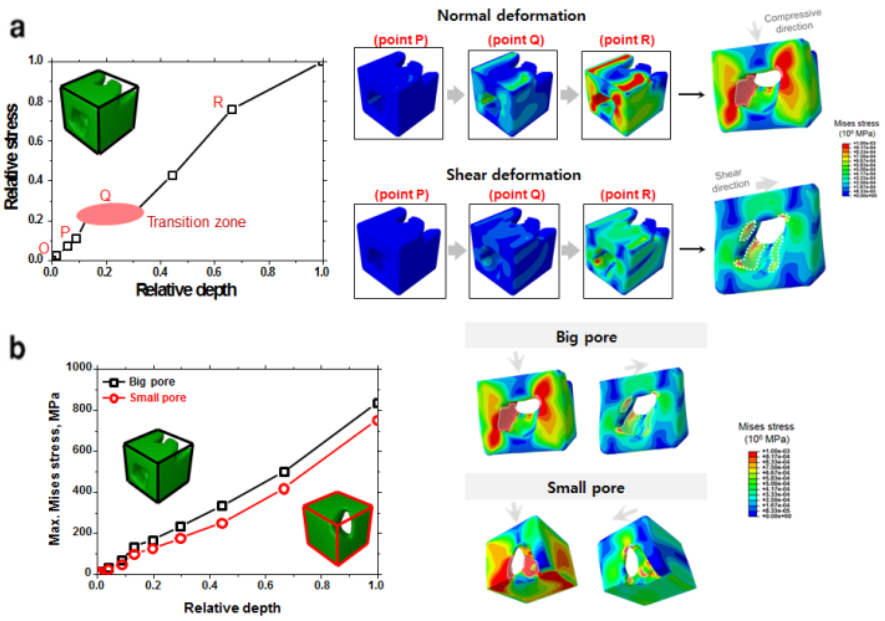

Figure 3. a) Comparison of deformation property between normal stress and shear stress on unit cell structure constructed using dual-level FE modeling. b) Theoretical modeling to different size of pore was confirmed to understand the effect or pore geometry on structural stability of porous material.

In order to distinguish PEG-HAP samples generated in this way from nonporous or randomly porous HAP blocks, we refer to the resultant interior structure as Aligned Multiple Capillary networks with gradually decreasing Diameter-HAP (AMCD-HAP). The porosities of the low- (pressure level 0~4), middle- (pressure level 4~8) and high- (pressure level 8~12) pressure sections of the AMCD-HAP during sintering were measured to be 7.60±1.35%, 9.33±0.94% and 13.49±3.89% based upon Archimedes' principle (n=3). By utilizing a micro-CT (ZEISS Xradia 510 Versa) with a resolution of 0.67 μm per pixel, we showed that pixels below the lower contrast threshold (corresponding to the low density characteristic of the material and thus the existence of many nano-channels inside the pixel region) were distributed throughout the AMCD-hap sample (Figure 4a), while most of these low-density pixels were interconnected with the exterior (Figure 4b). This method used to set the threshold in micro-CT based imaging, is based on experimentally determined data. The interconnectivity of these low-density pixels was 21.5%, 43.2% and 79.4% for the low (pressure level 0~4), middle (pressure level 4~8) and high (pressure level 8~12) pressure region of the AMCD-HAP, respectively.

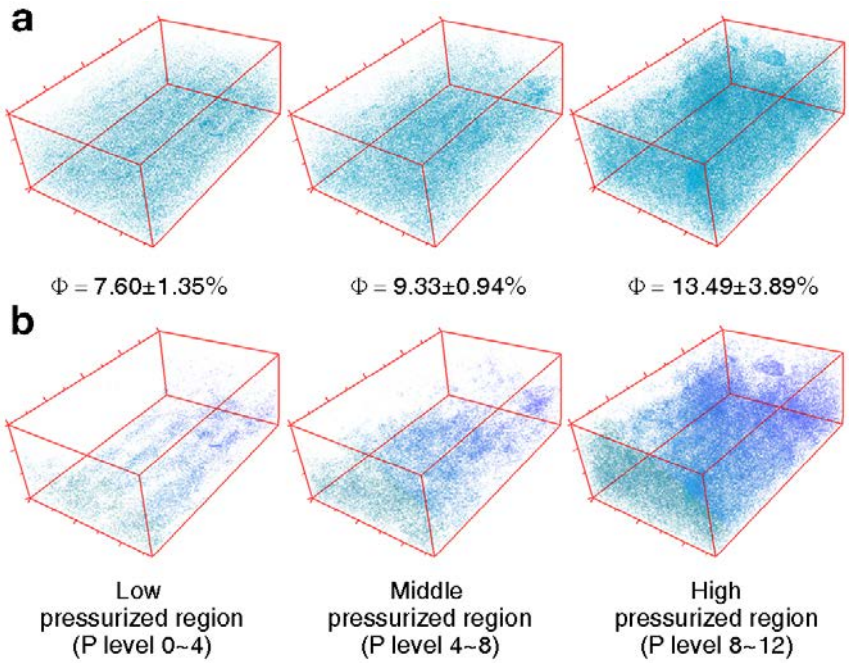

Figure 4. a) Distribution of low-density pixels (blue) in the low- (pressure level 0 ~ 4), middle- (pressure level 4 ~ 8) and high (pressure level 8 ~ 12) pressure regions in AMCD-HAP during sintering obtained from X-ray micro-CT analysis, where their porosities (Φ) were measured by Archimedes' principle to be 7.60±1.35%, 9.33±0.94% and 13.49±3.89%, respectively. b) Selected image of fully connected low-density pixels with exterior regions, as revealed by the X-ray micro-CT data.

Also, in order to observe nano-channels directly, AMCD-HAP species are divided into 4 parts along the pressure levels and FIB-FESEM tomography analysis was conducted. After then, surface 2-D images were converted 3-D images using the AMIRA program. As shown in Figure 5 a, b, when nano-channels are in the meddle-high level pressure and middle-low level pressure condition, blue region indicates empty space and gray region demonstrates ceramic space. Various sizes of pores are made depending on pressure and they construct 3-D networks. Moreover, we conducted HRTEM analysis to observe smaller nano-channels. As a result, we can see the nano-channels having the dozens of nanometers scale radii at the middle-low level pressure and we can find the part of the nano-channels which have 20 nm radii at the low pressure level condition (Figure 5 c, d).

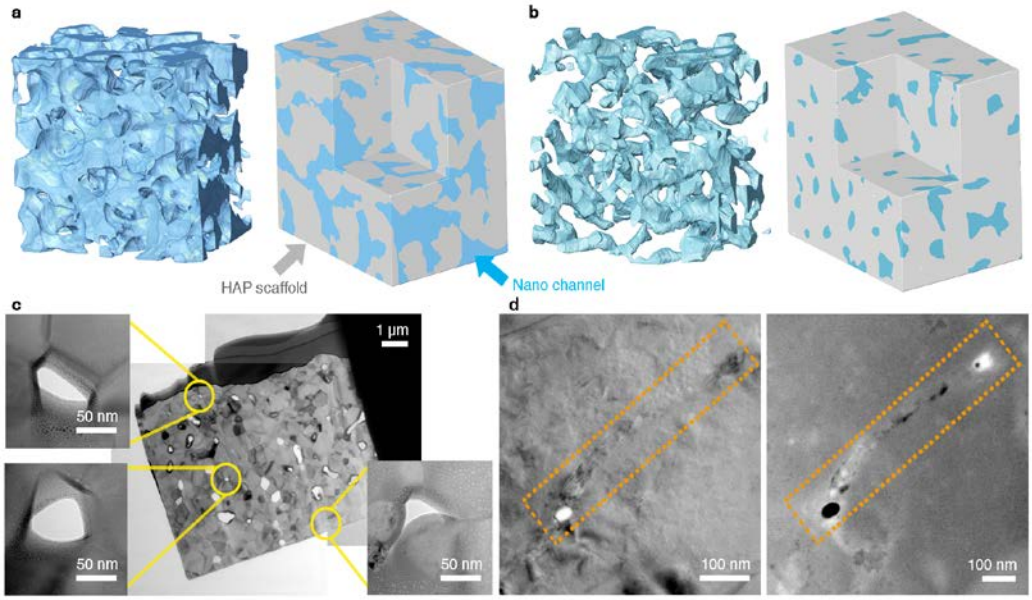

Figure 5. The nanoo-channels images were illustrated by using FIB-FESEM tomography. HRTEM images indicate the decrease of the nano-channels radii. a-b) Imaged AMCD-HAP regions at the middle-high and the middle-low level pressure condition, c-d) HRTEM images of nano-channels at the middle-low and low level pressure condition.

Additionally, after we analyzed the inner side of AMCD-HAP using nano-CT, we can observe a direct form of the nano-channels. By utilizing nano-CT data, we illustrated the images with the separation of the outside frame and the inner empty space. After that, we examined the connection of the pores. As a result, the 32.9% and 30.6% portion of pores were linked and formed porous networks caused by strong interconnection ability between pores (figure 6.). By making use of these results, we established nano porous networks inside bio-ceramics using gradient pressure technique. Also, we proved the presence of nano-channels inside AMCD-HAP structure which have high ability of interconnection and directionality and that the radii of nano-channels are changed gradually along pressure gradient.

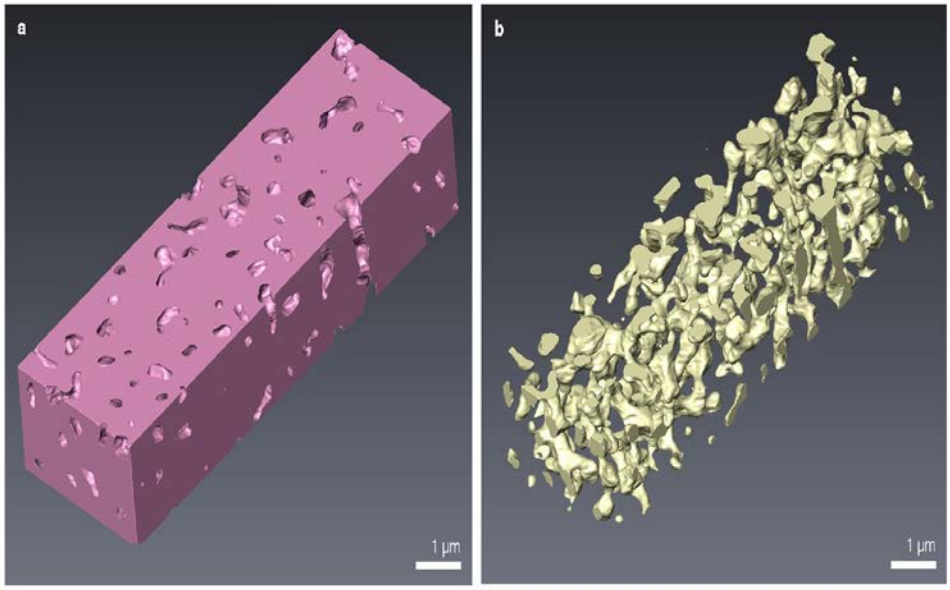

Figure 6. AMCD-HAP images using nano-CT. a) The frame image of AMCD-HAP. b) The inner empty space image of AMCD-HAP.

Using polarized optical microscopy (Olympus BX51), we directly visualized one of the two mechanisms that enabled the formation of our AMCD: phase separation between PEG and HAP. From the observation (Figure 7) we found that polymer agglomeration between PEG and HAP is dependent on thermal energy and pressure. These observations show that PEG converts into an ordered crystalline state after a melting-solidification process. After elevating temperature, pore is formed from PEG decomposition. By demonstrating the mechanism of nano-channel generation in ceramic, it was possible to control the porosity and interior structure of AMCD-HAP. Diverse structures of nano-channels have a great potential in tremendous kinds of applications such as mechanical machine, aerospace engineering.

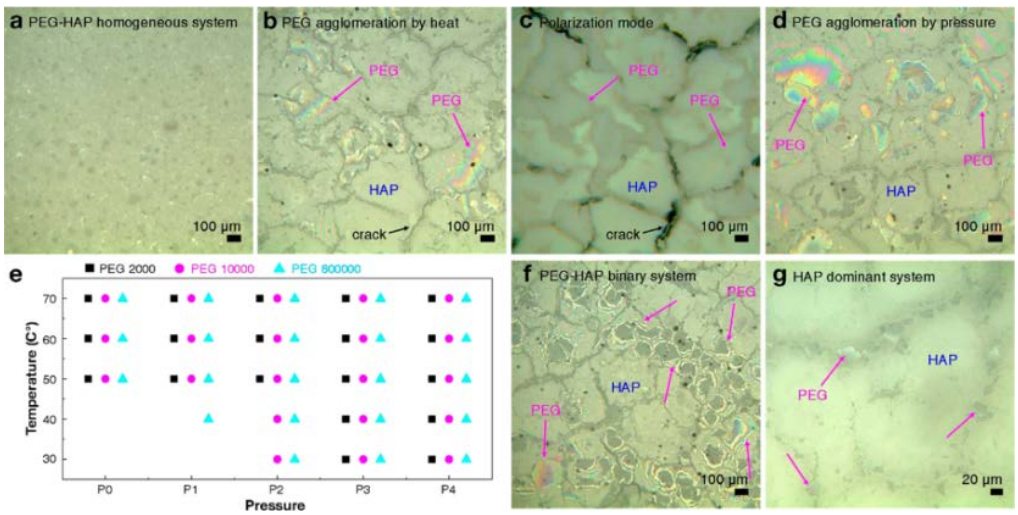

Figure 7. a) Homogeneously mixed state of PEG and HAP (1:10) at RT and atmospheric pressure. b) Sample shown in "a" after heating at 70 ℃ for 2 h. c) The color pattern of PEG material. d) When pressure from the 0.8 kg mass of metal cubes was exerted on the PEG-HAP mixture at 30 ℃ for 2 h. e) Polymer agglomeration chart of PEG-HAP mixture. f) Agglomerated PEG in a PEG-HAP binary system (1:1) at 70 ℃ for 2 h. g) Network of agglomerated PEG in a HAP ceramic dominant system (1:100) at 70 ℃ for 2 h.

Based on the confirmation of high connectivity of nano-channels in bioceramic, the capability of the AMCD-HAP to draw fluid was tested. As a control, nonporous HAP pellets and randomly porous HAP pellets, both made using non-pressurized sintering processes were tested and each showed no fluid transport. In contrast, the AMCD-HAP drew fluid very effectively from its reservoir at the base end of the pellet and delivered it to the upper surface located some 2 cm above the reservoir's fluid level. To visualize the interior capillary transport in situ and to assess the difference in fluid migration between the AMCD-HAP and the nonporous HAP pellets, ^{18}F-fluoro-deoxyglucose (FDG) positron emission tomography (PET) and computerized tomography (CT) scanning were performed (Figure 8). Each pellet was placed vertically in a sterile container filled with distilled water containing 18F-FDG and real-time images were acquired over a period of 60 minutes. In the AMCD-HAP pellet, 18F-FDG migrated through the aligned nano-channels of the pellet. In contrast, there was no migration of 18F-FDG in the nonporous conventional HAP pellet.

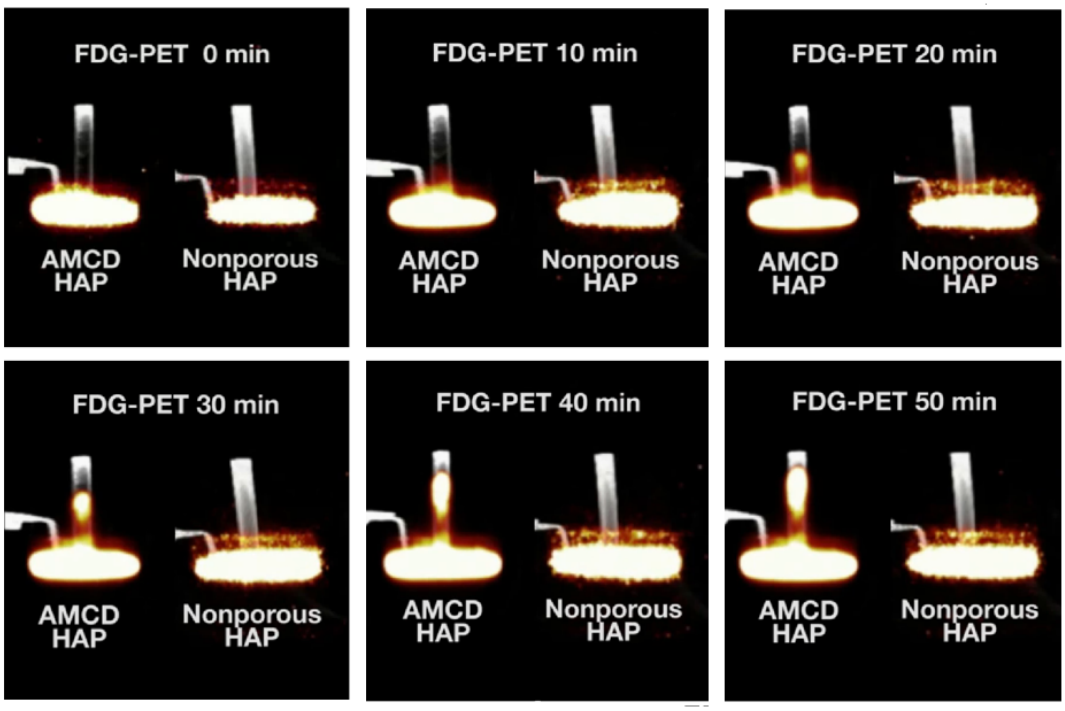

Figure 8. Fludeoxyglucose-positron emission tomography (FDG-PET) imaging showed that the AMCD-HAP sample (left) exhibited a greater capillary force than a control nonporous HAP sample (right).

Consistent with the physical geometries of aligned pore channels of varying diameters in the AMCD-HAP pellet, the CT image analysis showed a gradient of radiolucency along its length, overall being more radiolucent than the nonporous control pellet (Figure 9).

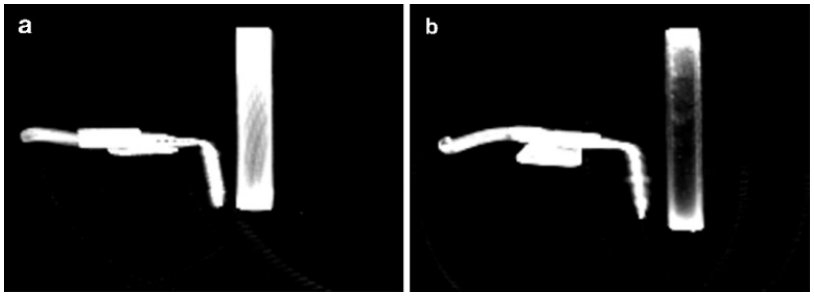

Figure 9. Computed tomography (CT) scanning of the inner hierarchy structure of the non-porous HAP compared to the AMCD-HAP pellets. a) Image corresponds to a solid HAP pellet and reveals an inner structure with few to no pores. b) Image corresponds to an AMCD-HAP pellet and reveals an inner structure with a gradient of porosity from one end to the other, corresponding to the pressure gradient applied during sintering (see Figure 4a). The x-ray beam of the CT scanner interacts with the HAP material, attenuating beam energy with increasing HAP density with a dense area recorded as a "bright" image.

For further quantitative comparison, AMCD-HAP, nonporous HAP, and randomly porous HAP samples were partially immersed in water in which a dye was dispersed to permit visualization of fluid flow. The rise of the dye-colored water was monitored and measured. The AMCD-HAP pellet, with its upwardly directed and narrowing channels, showed the fastest and the highest fluid rise (Figure 10). When the AMCD-HAP pellet was placed in an inverted position with the channels widening towards the top, it also drew water but at a slower rate and to a lower height. There was no water rise in the nonporous (Φ=0.19±0.07%) or homogeneously porous HAP pellets of low porosity (Φ=0.78±0.08%) as the pores were isolated from each other. For a more direct comparison, we made homogeneously porous HAP pellets with the same porosity (Φ=10.92±0=2.00%) as the porosity of the AMCD-HAP pellets (Φ=10.83±1.65%), by altering the initial ratio of PEG and HAP in the composite mix. The fluid transport test showed that the final capillary rise was only slightly better for the AMCD-HAP than the homogenously porous HAP pellet, the rate of transport was clearly faster in the AMCD-HA pellet, an outcome due to its tapered and hierarchical structure and high connectivity.

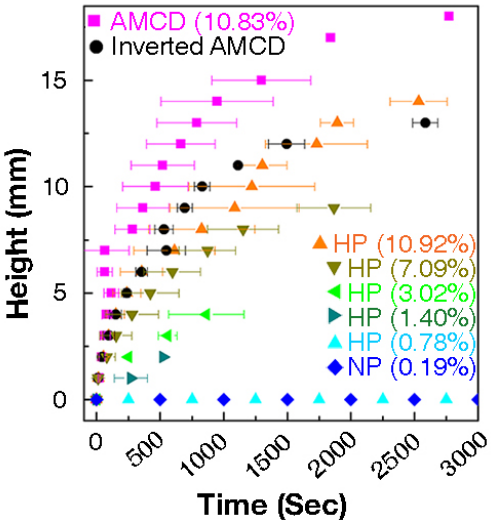

Figure 10. AMCD-HAP sample (magenta square), inverted orientation for AMCD-HAP sample (black circle), nonporous HAP sample made from HAP/PEG at a ratio of 0.01% by weight (blue diamond) and homogeneously porous HAP samples (triangles) with various porosities were compared for their abilities to draw fluid by capillary force in real time. The average porosity of each sample is indicated in brackets after their symbols.

Further tests were conducted on samples engineered to have different porosities, created by incorporating different amounts of PEG of variable chain length. The results in Figure 11a showed that the samples containing larger amounts of PEG before sintering exhibited a higher and faster capillary rise due to an increase in the amount of both large and small channels, and thus a greater overall porosity. In addition, by varying the molecular weight of the PEG polymer from 400 to 600000 g mol^{-1}, we were able to observe a correlation between the molecular weight of the polymer and the amount of capillary rise in the resulting AMCD-HAP pellet (Figure 11b).

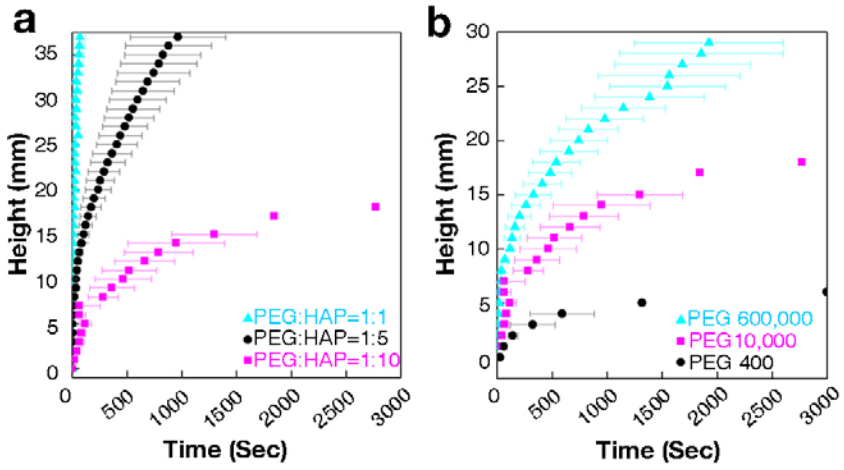

Figure 11. a) Comparison of capillary rise height among HAP samples sintered with different ratios of PEG polymer. PEG:HAP = 1:10 (magenta square), PEG:HAP = 1:5 (black circle), PEG:HAP = 1:1 (cyan triangle). b) Comparison of capillary rise height among HAP samples sintered with different molecular weights of PEG polymer. PEG MW 400 g mol^{-1} (black circle), PEG MW 10000 g mol^{-1} (magenta square), PEG MW 600000 g mol^{-1} (cyan triangle).

We attribute this correlation to the fact that PEG entangles more with itself and therefore agglomerates more when its molecular weight is larger. However, this result holds only for samples subjected to our pressurized sintering process; if the HAP-PEG mixture was sintered without additional pressure, the resulting pellets showed only small variation in porosity over a wide range of PEG molecular weight (Figure 12).

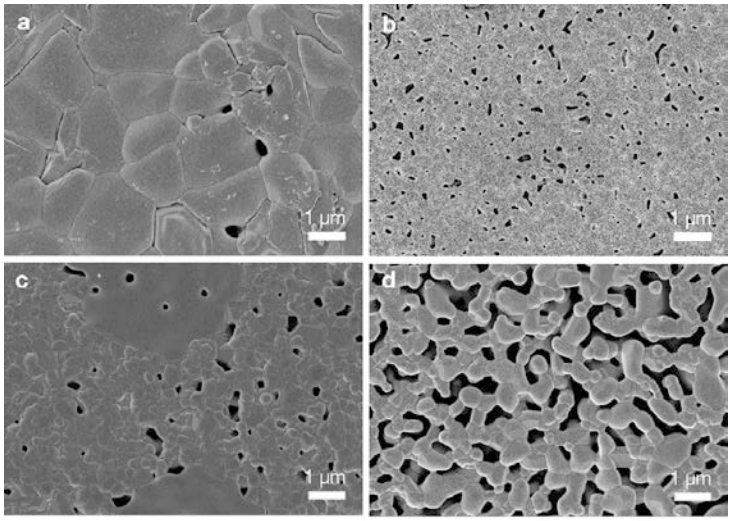

Figure 12. Porosity of the PEG-HAP pellet depends on the PEG molecular weight and applied pressure level during the sintering process. a) FESEM image of HAP and PEG 2000 molecular weight (MW) mixture after conventional sintering without pressurization b) FESEM image of HAP and PEG 600000 MW mixture after sintering without pressurization. **c)** FESEM image of HAP and PEG 2000 MW mixture after sintering under pressure. d) FESEM image of HAP and PEG 600000 MW mixture after sintering with pressurization. Chain length (corresponding to molecular weight) and pressure level are both important factors affecting phase separation. a, b) When the molecular weight of PEG was greater, the porosity of the HAP-PEG mixture increased slightly after conventional sintering. c, d) Pressure exerts a more important influence on porosity than does polymer molecular weight: porosity became significantly greater after sintering under pressure.

Based on these findings, we hypothesized that the AMCD-enabled HAP composite could mimic the vascular supply of nutrients provided by the terminal supply network of natural hard tissues found in biological systems. Among the circulatory systems of living organisms, bone is known for having a design that utilizes hierarchically organized tubes and gradually tapered channels to supply nutrients and growth factors to its resident cells. Alterations to this intrinsic hierarchy for internal transport can pose a challenge when bone must be fitted with an implant. Bone implant materials can fail to support cell growth when circulation is impaired due to a compromised interface between the implant material and the natural host bone impeding nutrient supply. Surgeons have identified the need for future implant designs to incorporate nanoscale structure to promote circulation rather than the millimeter or micrometer channels that are molded or machined into implants for fluidic

conduction in order to overcome this clinical limitation of bone implants. Therefore, it seemed natural to speculate that our AMCD-enabled HAP can address the issue of nutrient transport to the bone and implant interface so that it can be used as a future bone implant material with a built-in, self-powered transport network of highly aligned nano-channels to support bone cell growth and activity at the interface with the host tissue.

In pursuit of this vision, we attempted to test whether AMCD-HAP blocks can indeed support the metabolism of living cells by efficiently supplying fluids and nutrients along the length of the material from a source restricted to the opposite end. To this end, we tested the survival, growth and gene expression activity of human bone cells grown on the surface of the AMCD-HAP pellet, centimeters away from the media fluid reservoir. In these tests, an AMCD-HAP pellet was placed standing vertically up (nano-channels narrowing towards the top) in a sterile container filled with cell culture media, along with a control non-porous, but otherwise identical control HAP pellet, for comparison. Human-derived osteoblast cells (Lonza Clonetics) were seeded on the top surface of each pellet at a density of 1×10^5 cells ml-1, where the surface area was approximately 7 mm×2 mm. Containers were tightly sealed to prevent evaporative transport and maintained at 37 °C in an ambient atmosphere with 5% CO_2. The top surface of either of the HAP pellets upon which the osteoblast cells were seeded was approximately 1 cm above the nutrient media, as illustrated in Figure 13. In this geometry, the osteoblast cells were maintained at the humidified air interface, with the only source of nutrients being drawn through the highly aligned nano-channels of the AMCD-HAP ceramic over a distance of 1 cm. As the system inside the container maintained a vaporization-liquefaction process, capillary action was able to continue by the evaporative loss at the surface of the HAP pellet, as well as by the cells incorporating the transported nutrients for their growth, proliferation and differentiation.

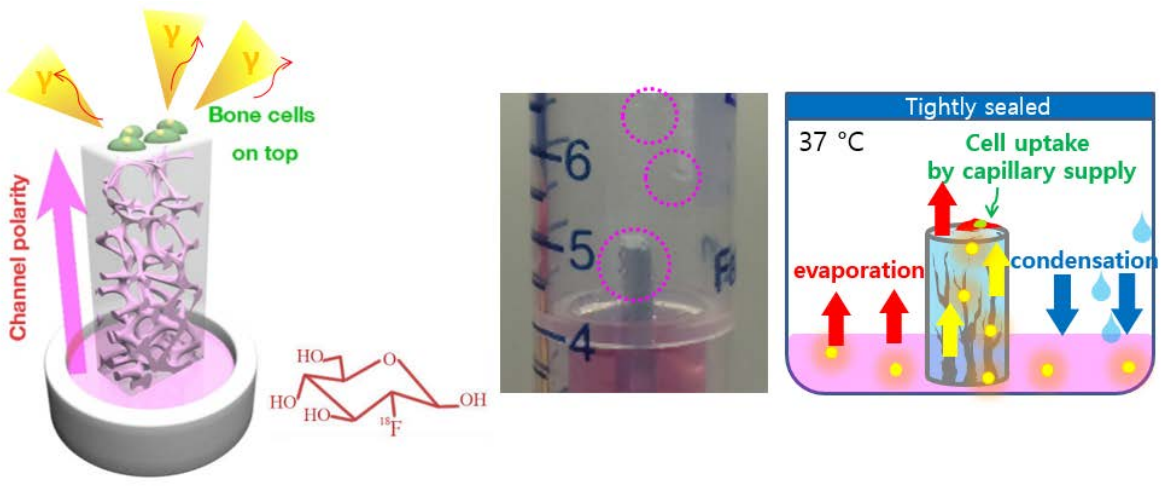

Figure 13. Schematic representation of the method of seeding human osteoblasts onto the top surface of AMCD-HAP samples (left) and image of experimental system (middle). Based on the formation of droplets on the surface of container wall (magenta circle in the middle image), we assumed that the system maintained vaporization-liquefaction process (right).

To directly confirm nutrient transport through AMCD-HAP capillary channels, we detected cellular uptake of radioactive 18F-fluoro-deoxyglucose (^{18}F-FDG) material by a gamma detector. After growing cells on top surface of AMCD-HAP in the air-exposed state for 24 hours, we exchanged media to a low glucose formulation to restrict cells for glucose (Dulbecco's Modified Eagle's Medium with 1.0 g L-1 Glucose, without L-Glutamine : FBS : Penicillin-Streptomycin=90.1%: 9% : 0.9%), and after 24 hours, added 18F-FDG in aqueous solution to the bottom reservoir and collected the radio-labeled cells 1-hour later. At this point, as shown in Figure 14a, the number of cells was nearly 5 times greater for the AMCD-HAP pellet (1773±316, n = 3) than that of nonporous HAP pellet (370±210, n = 3). In addition, as shown in Figure 14b, from the gamma detection analysis, the uptake and incorporation of 18F-FDG by these cells growing on the AMCD-HAP sample was orders of magnitude greater (20330.1±2053.7, n = 3) than that of the nonporous HAP sample (594.9±120.2, n = 3). These results indicate that transport of 18F-FDG and cellular uptake was greatly enriched in the AMCD-HAP samples.

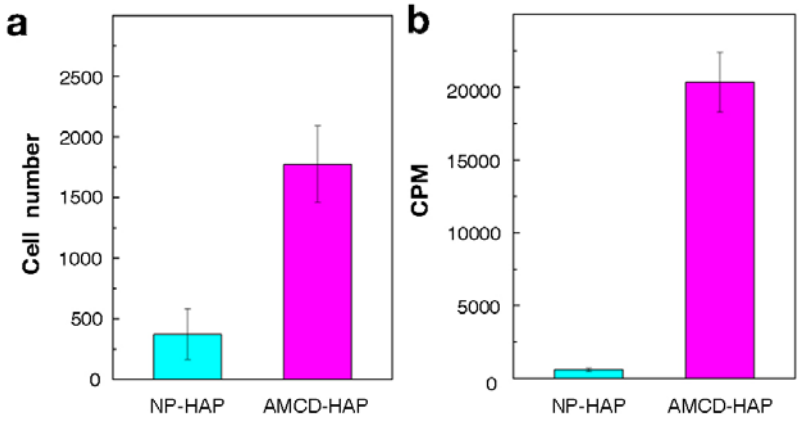

Figure 14. a) Cells grown on the top surface of AMCD-HAP, after 2 days of relying on the nutrient supply by nano-channels, showed a much greater number of cells (proliferation) than were grown on the top surface of nonporous HAP samples. b) Cellular uptake of ^{18}F-FDG on the top surface of AMCD-HAP was measured as orders of magnitude greater than the uptake and utilization of ^{18}F-FDG by cells grown on the nonporous HAP samples.

To ascertain that human bone cells grown on the capillary-delivery surface of the AMCD-HAP pellet not only survive, but also maintained their differentiated phenotype for bone matrix production, the gene expression profiles for several bone-related proteins were assayed and compared to human osteoblast cells grown at the air to media interface atop the

nonporous HAP as the control. Messenger RNA (mRNA) levels for the two were estimated using the standard technique of reverse transcription of mRNAs to complementary DNA strands followed by real time quantitative PCR analysis (RT-qPCR). Using this approach, the relative abundance of the mRNAs for selected bone matrix genes was quantified as shown in Figure 15. After 48 hours of cell growth that depended solely on nutrient supply through the nano-channels of the AMCD-HAP, we found that the mRNAs for bone matrix-related proteins were actively expressed with expression levels comparable to those of control osteoblasts. The data from the RT-qPCR analysis indicated that the microenvironment created at the AMCD-HAP surface supported osteoblast cell gene expression in a manner equivalent to the standard technique of culturing bone cells at the media to air interface on a nonporous HAP surface.

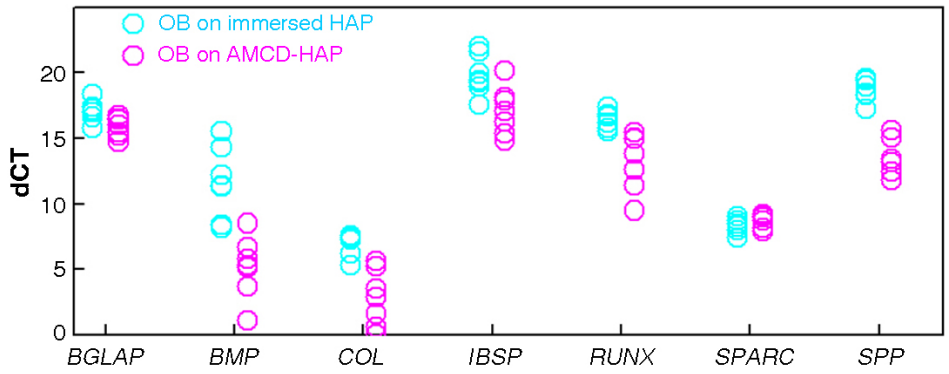

Figure 15. Relative gene expression measured by quantitative real time PCR revealed that osteoblasts grown on top of AMCD-HAP samples (magenta, n = 7) expressed similar levels of bone-related genes compared to the expression profile for osteoblast cells grown on HAP material at the media to air interface as control (cyan, n = 7).

After variable culture periods, the nuclei and actin cytoskeleton fibers were stained with DAPI and phalloidin, respectively, and the cells were observed using fluorescence microscopy. Notably, as shown in Figure 16, the surface of the AMCD-HAP pellet showed vigorous osteoblast cell growth, whereas few osteoblast cells survived on the nonporous HAP pellet. Cell proliferation is an increase in cell number and it is also an increase in the mass of new cells growing on the transport active surface of the AMCD-HAP pellet. The increased mass of the cells comes at the expense of the nutrients in the media that are transported through the AMCD-HAP to the cells. The cell proliferation, gene expression and 18F-glucose incorporation into cells demonstrate through corroborative approaches that nutrient supply through the aligned hierarchically connected nano-channels was sufficient for these specialized osteoblast cells to proliferate and differentiate.

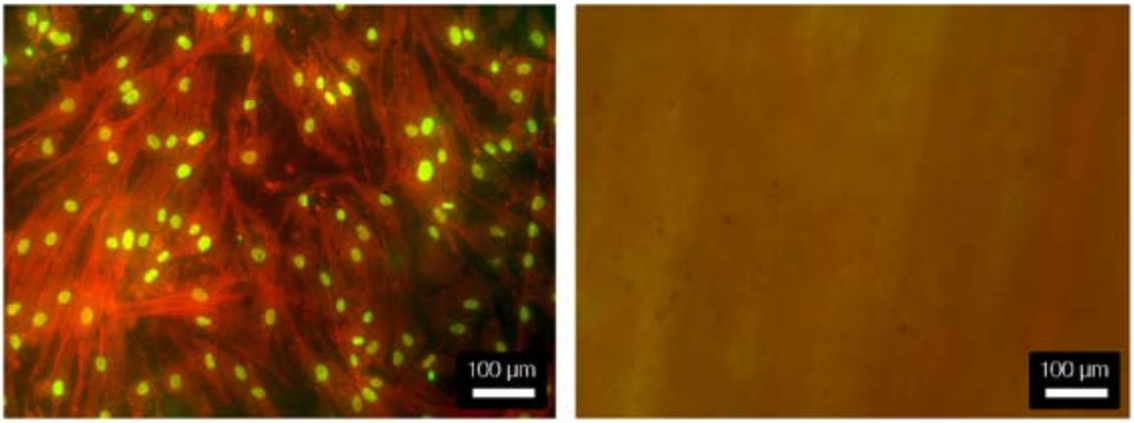

Figure 16. After 1 week, osteoblasts were observed growing on the surface of the AMCD-HAP samples, as shown by fluorescence microscopy (left). On the contrary, there was no cell on the surface of nonporous HAP samples with identical experimental condition (right).

Looking towards the future, by mimicking transport pathways of natural bone in a ceramic HAP material with aligned and diameter-graded nano-channels which increase fluid and nutrient circulation, one can envision a pathway for the next generation of bone implants, which could become 'alive' with their built-in hierarchical networks of biocapillary-like supply. While incorporating AMCD-HAP into bone implants stands out as an attractive possibility, the findings in this work could have a broader impact in other areas as well, such as lubrication in ceramic motors, fuel transport and energy conversion. Furthermore, it is known that living organisms metabolize most efficiently when resources are distributed throughout their tissues by a fractal network, resulting in minimal energy dissipation. In our research, networks of gradually tapering nano-channels showed similarly distributed and self-powered supply for bone cells to proliferate and maintain their specialized gene expression profile. This work also introduced a novel and reproducible manufacturing technique for constructing such networked nano-channels within a ceramic biomaterial making use of pressure-gradient induced differentiations to phase-segregation between PEG and HAP.

US side: led by Brown University, with support in materials and data from SNU

Experiment:

In addition to collaborate with and support the SNU team in conceptualization, design, and theory analysis of the pursuits reported above, the Brown team has taken on the challenge of developing a second pathway for building into ceramic composites 3D hierarchical networks of capillaries and for functionalizing them with additional capabilities.

HAP (Hydroxyapatite: $Ca_{10}(PO_4)_6(OH)_2$) was synthesized by the precipitation method with calcium hydroxide ($Ca(OH)_2$, 99.0%, High Purity Chemical, Japan) and phosphoric acid (H_3PO_4, 85.0%, Junsei Chemical Co., Ltd) in aqueous base [19]. In distilled water, 0.5 M of $Ca(OH)_2$ was prepared. After stirring vigorously with a mechanical stirrer (overhead stirrer MSM-1 Jeio Tech) for an hour, 0.5 M of H_3PO_4 was added drop-by-drop using a digital burette (Metrohm 876, Dosimat Plus). The final composition ratio of $Ca(OH)_2$ and H_3PO_4 was 10:6 and the precipitants were aged for 24 hours while stirring at room temperature. The HAP solution was filter-pressed and freeze-dried. Dried HAP powder was mixed with agarose gel powder (Sigma Aldrich) in DI water and sonicated to make homogeneous colloidal mixture. The colloidal mixture was heated to 80 °C for 1 hour in an oven and cooled down to room temperature. The HAP-gel composite was dried and sintered at 1100 °C for 2 hours. A baseline weight ratio of HAP and agarose gel was set at 5:1 (and 2 wt% of agarose gel in water) in our standard mixture. By changing the weight ratio, different porosities and capillary pore sizes is obtained in the same sintering process. By stacking HAP-agarose gel composites of gradually changing weight percentage of agarose gel, one can then obtain a gradient porous material with built-in networks of capillary channels tapered from one end to the other. Within a micro- or nano-scale capillary, the Laplace force that is inversely proportional to the diameter has been shown to be strong enough to power continued transport of bio and viscose fluids [20].

To add a self-regulation mechanism onto the self-powered supply of lubricants or biomolecules, one could make use of another phase-changing effect that is achievable in a number of polymers. One such phase-changing polymer is poly(N-isopropylacrylamide) (PNIPAM) whose phase-change is one of changing hydrophilicity at a temperature in the convenient range of body-temperature [21, 22]. It changes phase from being hydrophilic to hydrophobic when its temperature is raised above this temperature. In the proof-of-concept tests, one end of the capillaries in the fabricated composite was filled with the PNIPAM whose phase-changing temperature was kept at its normal 32 °C, which is however

changeable via altering the co-polymer structure. The phase-change is accompanied with a volume-change from being swelled in its hydrophilic state (below 32 °C) to half of that volume in its hydrophobic state (above 32 °C). With this volume change the payload (lubricant, coolant, or biomolecules) would be secreted (squeezed) out much like the sweat secretion by sweat gland in human skin. For direct visualization of the self-regulated release and subsequent self-powered transport of coolant or the 'payload' to the terminal top surface, a composite block fabricated in the process described above was pre-loaded with the aqueous mixture solution of PNIPAM (10 mg/ml, Sigma Aldrich) and fluorescent dye, fluorescein isothiocyanate (FITC) (0.5 mM, Sigma Aldrich). Its outer surface was thoroughly rinsed and cleaned to remove any residual of the polymer mixture adhered to the surface during the process. It was then dried out. It was observed by inverted fluorescence microscope (Leica) to ensure that PNIPAM/FITC was loaded into the nanopores of the composite and that no residual was left outside before the release mechanism was activated. Prior to the self-regulated release (secretion) tests, the sample was first placed into water that was kept at below 32 °C. The sample was subsequently heated in water to 60 °C. Released FITC in the water was collected every 5 min and fluorescence intensity was quantitatively measured using fluorometer (Cary Eclipse). Test results validated the concept and design of self-regulated release and are presented in details in the section below.

To assess the potential of our new HAP composite forming method for fabricating structures of multi-functionality and shapes, we fabricated various forms of the HAP composites, including ones mixed with reduced graphene oxide for remote control by inductive heating. Figure 17 shows examples of large size HAP composite cylinders, squares, wedges with and without central hole, and graphene-reinforced HAP composites (grey, right-most of 2nd row of middle part). Moreover, we confirmed that magnetic nanoparticle of iron oxide can be readily, homogeneously incorporated into HAP composite (not shown in Figure 17).

These highlight the many advantages of this fabrication approach: its ease to mould and to machine the structures into components and devices of various shapes, sizes, and functionalities. It is also readily extendable to further incorporation of other materials to enable new functions that may not be found in Nature. For example, reduced graphene oxides and magnetic nanoparticles incorporated into the composites would allow the electrical and thermal properties of HAP composites to be tuned for applications in which the temperature-regulated release of payload (e.g. drug, coolants, lubricants and even Li+ ions) activated and controlled by inductive heating in remote. Such composites also allow for in

situ NMR imaging (CT) for the inspection of the state of the grafted HAP composite. This HAP/agarose gel method is also biocompatible and environmentally friendly.

In future studies, porosity control by controlling weight ratio of HAP and agarose can be implemented as well, whose success would open door to the creation of hierarchical networks of capillaries of varying sizes and densities in designated spatial regions.

Figure17. Photographs of fabricated HAP composite and molded structures that are ready to be machined into ceramic mechanical parts.

Microscopic morphology of synthetic composite samples was imaged by scanning electron microscope (SEM) (LEO 1530-vp). Figure 18 shows the SEM image of synthesized HAP in the pre-sintering compressed powder state (Fig. 18a), low magnification (Fig. 18b) and high magnification of the sample after sintering at 1100 °C for 2 hrs (Fig. 18c) . The as-synthesized HAP image shows nano-needle-like fluffy powders, which is a general characteristic of the synthetic method we used [19]. The samples after sintering showed micro- and nano- porous channels (capillary) in the SEM cross-sectional view, which extend into the 3D volume and form interconnected 3D networks, as have been established in earlier 3D tomography and fluid transport experiments reported in [23]. The pore diameter in the SEM ranged from ~100 nm to ~1 um. (Fig. 18b and 18c) Porosity of 45% was obtained by a water infiltration method, also called imbibitions method [24]. Briefly, volume and weight of original bone were measured, water was infiltrated into the composite sample, and weight of bone/water was measured. From the difference of weight between dried and wetted composite, infiltrated water weight and volume was calculated. More precise porosity can be measured by micro-CT.

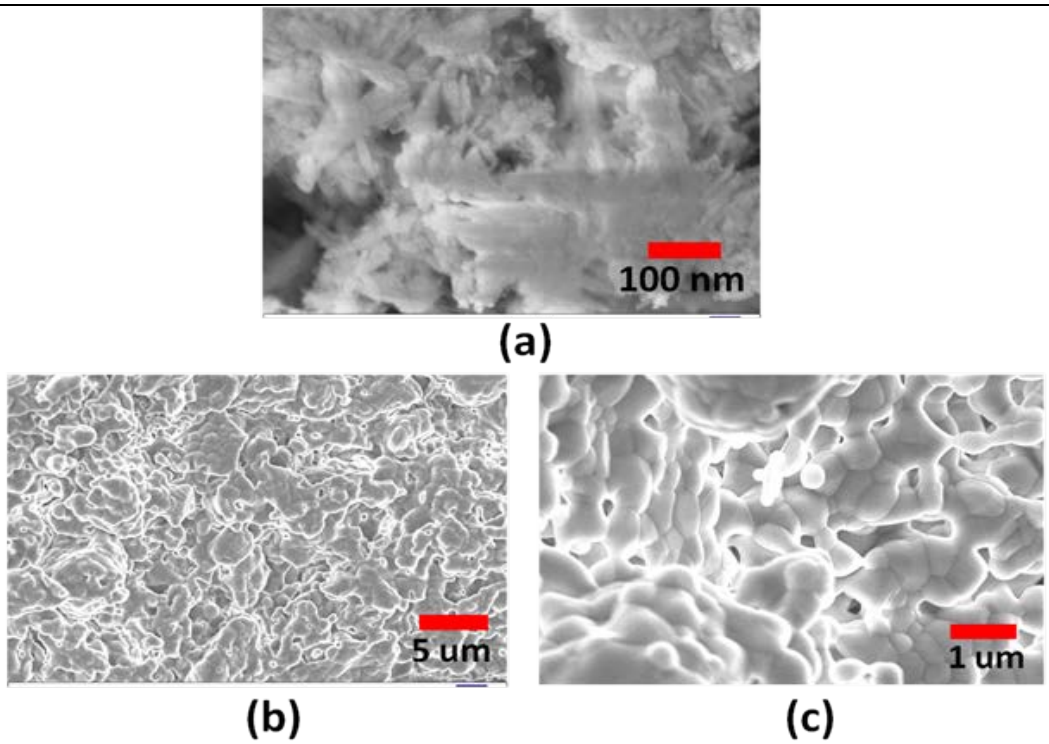

Figure 18. SEM image of HAP composite: a) as-synthesized HAP powder, b) low magnification image of the composite, and c) high magnification image. The weight ratio of HAP and agarose is 5:1 and sintered at 1100 °C for 2 hrs.

In examining whether the PNIPAM/FITC was infiltrated via the capillary networks into the cylindrical HAP composite sample (diameter = 10 mm and height = 20 mm) uniformly, using inverted fluorescence microscope, post-infiltration samples were cut at the middle and fluorescence images were taken from center to edge with 2 mm spacing. (Fig. 19)

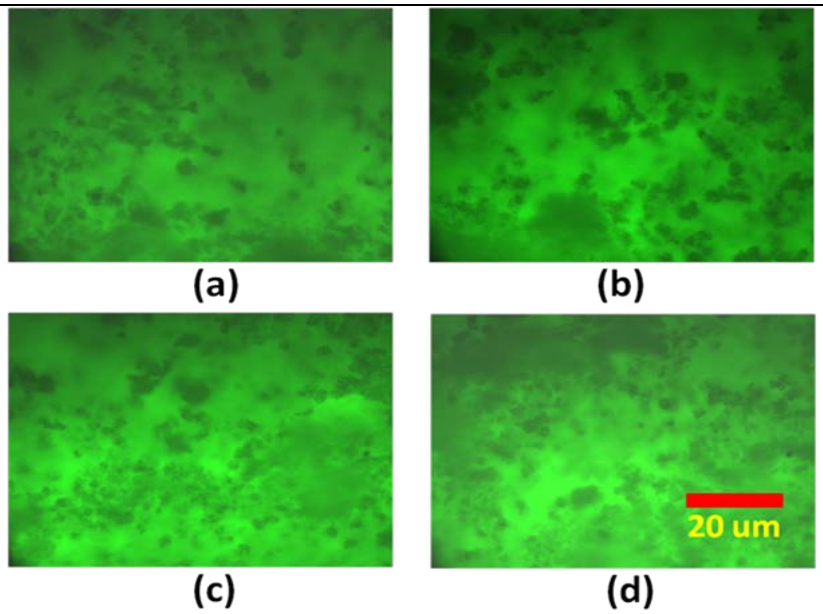

Figure 19. Cross-sectional fluorescence image of an HAP composite block infiltrated with PNIPAM/FITC: a) center position, b) 2 mm, c) 4 mm, and d) 6 mm away from center.

Figure 19a was taken at the center position, Fig. 19b at 2 mm away from the center, Fig. 19c at 4 mm away from the center, and Fig. 19d at 6 mm away from the center. These figures show uniformly distributed green fluorescence throughout the whole HAP composite sample and dark spots indicate the solid HAP without fluorescent molecule and PNIPAM. Laser confocal microscope may also be adopted for more detailed analysis of infiltration. The composite infiltrated with PNIPAM/FITC released FITC at temperature above the PNIPAM's phase-changing temperature 32 °C.

Test of Self-regulated Release: A further demonstration of the self-regulated release and transport of lubricant (FITC), a HAP composite was placed on top of a FITC-containing PNIPAM container at room temperature and then temperature was gradually raised to 55 °C (Fig. 20) At room temperature, there was no release of FITC (left-most photo of Fig. 20). With the base heater temperature rises up to 55 °C, FITC was released by the phase transition of PNIPAM and transported upward through HAP composite by capillary force.

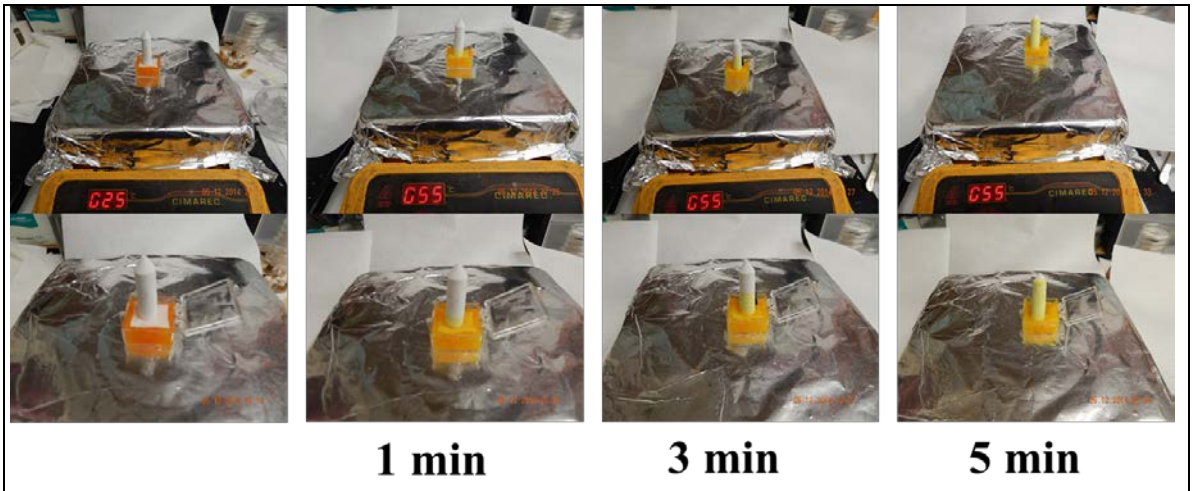

Figure 20. Controlled release of fluid and spontaneous delivery of the fluid through nano-capillary network of HAP composite. Lower image is the magnified image of corresponding upper image for clarity.

For a quantitative assessment of the release rate and kinetics, we placed a sample in 60 °C water collected every 5 minutes the fluorescence spectra and intensities of the FITC-containing fluid that was secreted by the PNIPAM and transported by the capillary force from inside the sample to surface and then into water. The fluorescence intensity was measured using fluorometer (excitation wavelength = 480 nm, Cary Eclipse). (Fig. 21a)

In a control experiment, the FITC release by diffusion (osmosis) was carried out at room temperature (Fig. 21b, red curve). Fig. 21a displays the time evolution of the spectra of the FITC released at 60 °C. Fig. 21b compares the FITC spectral-peak intensity change over time as the sample temperature rose to 60 °C (black curve) and that of a sample kept at room temperature (red curve). The release at temperatures above the PNIPAM's phase-change temperature is clearly much faster, by ~250%, than that of osmosis diffusion.

The storage (or loading) capacity of the payload (e.g. FITC) of the composite can be estimated by calculating the weight difference between raw dried ceramic composite and the infiltrated one with 0.5 mM FITC and 10 mg/ml PNIPAM. With a cylindrical sample of diameter = 10 mm and height = 20 mm, the payload of FITC was 0.35 umol. At 60 °C, 10% of FITC was released in 5 min and 30% in 40 min, after 40 min the release tapered down. At room temperature, it was 5% in 5 min, 9% in 40 min and 15% in 120 min. The release profiles above phase changing temperature can be controlled or optimized by changing sample size, porosity, concentration of infiltration solution, surface-grafting of PNIPAM, etc.

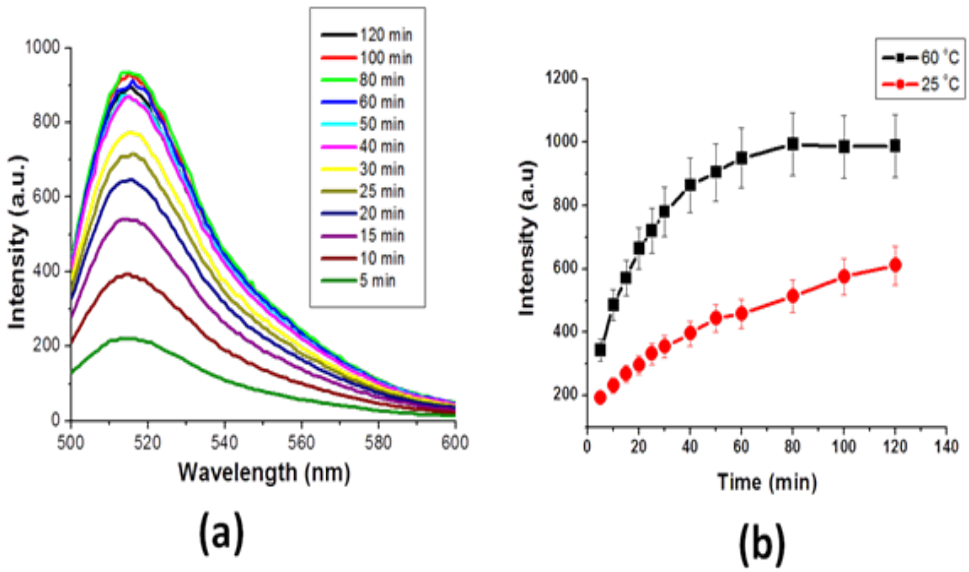

Figure 21. Releasing profile of FITC from HAP composite infiltrated with PNIPAM/FITC: a) fluorescence spectra taken at 60 °C and b) peak intensity change with time, black curve from 60 °C and red one from room temperature.

Multi-functional HAP composites with swelling polymer, magnetic nanoparticles, carbon nanotubes, and titanium dioxide/silver were successfully prepared, and Fig. 22 shows their functional properties. In further study, one could investigate the microscopic properties and detailed functionalities of those composites and their dependences on compositions and preparation methods.

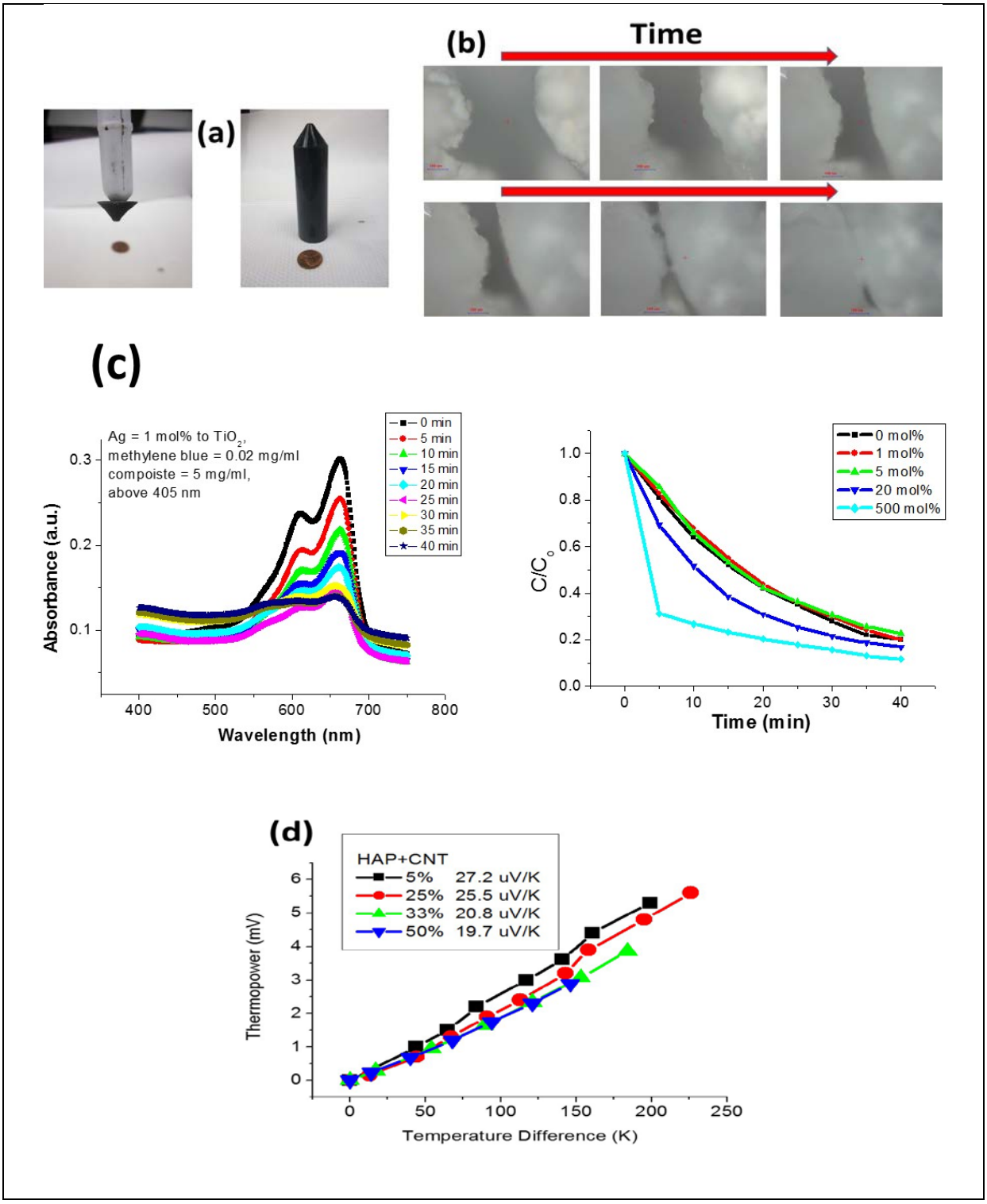

Figure 22. (a) left; HAP/magnetic nanoparticle, right; HAP/carbon nanotube-thermally and electrically conductive bone composite, (b) self-healing composite of HAP/swelling polymer; with self-powered water supply the crack is sealed, (c) photocatalytic HAP composite with TiO2/Ag, left; photocatalytic decomposition of organic pollutant-methylene blue with visible light illumination dependent on time, right; composition-dependent photocatalytic efficiencies, (d) HAP/carbon nanotube; thermal energy harvesting; the composite shows high Seedbeck coefficient (values in box), which is comparable to pure CNT and promising for thermoelectric materials.

Summary:

Made by a new relatively simple and readily scalable fabrication method, the structured composites with networks of micro- and nano-scale capillaries built in during sintering can be expected to enable both biomedical and mechanical applications. In the former, these composites have enabled a conceptual demonstration of the feasibility of incorporating a self-regulated release mechanism together with the self-powered transport of fluid through capillary networks from one end to the other. In the latter, they have brought us a step closer to solving a particular problem in ceramic rotors and engines, namely, self-cooling and self-lubrication, like in human knees.

The synthesis method offers many advantages such as biocompatibility, easy preparation, scalable preparation, and readily-mouldable into various shapes such as cylinder, square, rod, thin plate as small as a micrometer. Porosity control can be achieved by controlling the weight ratio of HAP and agarose, and thus also possible to form continuously gradient porous structure.

Self-regulated release of 'payload' was demonstrated with a fluorescent molecule pre-loaded with a phase changing polymer (PNIPAM) into the fabricated HAP composite. Above the phase changing temperature of the PNIPAM, the polymer changes its phase from hydrophilic to hydrophobic and thereby secretes its payload (e.g. lubricants, coolants, or healing agents) which then gets transported to the terminal surface along with the fluid via the capillaries by the Laplace (capillary) force. This built-in mechanism of autonomous supply of desired fluids to the designated surface of the ceramic part could complement and be coupled to an external resupply mechanism in the periphery for sustainable operation.

Although the operation mechanism is generally applicable, beyond autonomous lubrication in ceramic rotors and valves, to bio-mechanics, e.g. synthetic joints, skeletal repairs, thermal management of embedded electronics, as well as drug delivery, pulling these mechanisms and components together in one ceramic composite system requires understanding the conflicting demands and constraints of particular applications. To that end, we see the need for further studies, both experimental and theoretical, as well as application-specific designs and tests.

REFERENCES

[1] Bejan, A. and Lorente, S., "Constructal theory of generation of configuration in nature and engineering", J. Appl. Phys., 100, 041301, (2006).

[2] Drucker, D. A., Capello, W. N., D'Antonio, J. A., and Hile, L. A., "Works in progress #6. Total hip arthroplasty using a hydroxyapatite-coated acetabular and femoral component", Orthop. Rev., 20, 179–185 (1991).

[3] Deeb, M. E., Hosny, M., and Sharawy, M., "Osteogenesis in composite grafts of allogenic demineralized bone powder and porous hydroxyapatite", J. Oral Maxillofac. Surg., 47, 50, (1989).

[4] Jahn, A. F., "Experimental applications of porous (coralline) hydroxyapatite in middle ear and mastoid reconstruction", Laryngoscope, 102, 289, (1992).

[5] Christoffersen, J., Christoffersen, M. R., Larsen, R., and Møller I. J., "Regeneration by surface-coating of bone char used for defluoridation of water", Water Res., 25, 227, (1991).

[6] Walsh, W. R. and Guzelsu, N., "Compressive properties of cortical bone: mineral-organic interfacial bonding", Biomaterials, 15, 137, (1994).

[7] Koutsopoulos, S., Kontogeorgou, A., Petroheilos, J., and Dalas, E., "Calcification of porcine and human cardiac valves: testing of various inhibitors for antimineralization", J. Mater. Sci. Mater. Med., 9, 421, (1998).

[8] Nancollas, G. H., "Enamel apatite nucleation and crystal growth", J. Dent. Res., 58B, 861, (1979).

[9] Dalas, E. and Koutsoukos, P. G., "Crystallization of hydroxyapatite from aqueous solutions in the presence of cadmium", J. Chem. Soc. Farad. Trans., 85, 3159, (1984).

[10] Koutsopoulos, S., Demakopoulos, I., Argiriou, X., Dalas, E., Klouras, N., and Spanos, N., "Inhibition of hydroxyapatite formation by zirconocenes", Langmuir 11, 1834, (1995).

[11] Boskey, A. L. and Bullough, P. G., "Cartilage calcification: normal and aberrant", Scan. Electron Microsc., pt II, 943, (1984).

[12] Weiner, S. and Wagner, H. D., "The material bone: structure-mechanical functions relations", Ann. Rev. Mater. Sci., 28, 271, (1998).

[13] Giannoudis, P. V., Dinopoulos, H., and Tsiridis, E., "Bone substitutes: An update", Injury, Int. J. Care Injured, 36, S20, (2005).

[14] Hutmacher, D. W., "Scaffolds in tissue engineering bone and cartilage", Biomaterials, 21, 2529, (2000).

[15] Hollister, S. J., "Porous scaffold design for tissue engineering", Nat. Mater., 4, 518, (2005).

[16] Kieback, B., Neubrand, A., and Riedel, H., "Processing techniques for functionally graded materials", Mater. Sci. Eng. A, 362, 81, (2003).

[17] Pompe, W., Worch, H., Epple, M., Friess, W., Gelinsky, M., Greil, P., Hempel, U., Scharnweber, D., and Schulte, K., "Functionally graded materials for biomedical applications", Mater. Sci. Eng. A, 362, 40, (2003).

[18] Hing, K. A., Best, S. M., and Bonfield, W., "Characterization of porous hydroxyapatite", J. Mater. Sci. Mater. Med., 10, 135, (1999).

[19] Bouyer, E., F. Gitzhofer, F., and Boulos, M. I., "Morphological study of hydroxyapatite", J. Mater. Sci.: Mater. Med., 11, 523, (2000).

[20] Barber, R. W.; Emerson, D. R., "Optimal Design of Microfluidic Networks Using Biologically Inspired Principles", Microfluid. Nanofluid., 4, 179, (2008).

[21] Graziano, G., "On the temperature-induced coil to globule transition of poly-N-isopropylacrylamide in dilute aqueous solutions", Int. J. Biol. Macromol., 27, 89,

(2000).
[22] Jones, C. D. and Lyon, L. A., "Shell-restricted swelling and core compression in poly(N-isopropylacrylamide) core-shell microgels", Macromolecules, 36, 1988, (2003).
[23] Jang, H. L., Lee, K., Kang, C. S., Lee, H. K., Ahn, H. –Y., Jeong, H. –Y., Park, S., Kim, S. C., Jin, K., Park, J., Yang, T. –Y., Kim, J. H., Shin, S. A., Han, H. N., Oh, K. H., Lee, H. –Y., Lim, J., Hong, K. S., Snead, M. L., Xu, J., and Nam, K. T., "Nano-capillary self-powered nutrient supply in a ceramic biomaterial", ACS Nano (under revision)
[24] Dullien, F. A. L., "Porous Media. Fluid Transport and Pore Structure", Academic Press, (1992).

List of Publications and Significant Collaborations that resulted from your AOARD supported project:

a) Papers published in peer-reviewed journals

1. H. L. Jang, G. B. Zheng, J. Park, H. D. Kim, H. R. Baek, H. K. Lee, K. Lee, H. N. Han, C. K. Lee, N. S. Hwang, J. H. Lee and K. T. Nam, "In Vitro and In Vivo Evaluation of Whitlockite Biocompatibility: Comparative Study with Hydroxyapatite and β-Tricalcium Phosphate", *Adv. Healthc. Mater.*, 5, 128, 2016.

2. E. Toomey, J. Xu, S. Vecchioni, L. Rothschild, S. Wind, and G. E. Fernandes, "Comparison of Canonical versus Silver(I)-Mediated Base-Pairing on Single Molecule Conductance in Polycytosine dsDNA", *J. Phys. Chem. C*, 120, 7804, 2016.

3. S. W. Ha, H. L. Jang, K. T. Nam and G. R. Beck, "Nano-hydroxyapatite modulates osteoblast lineage commitment by stimulation of DNA methylation and regulation of gene expression", *Biomaterials*, 65, 32, 2015.

4. H. L. Jang, H. K. Lee, K. Jin, H. –Y. Ahn, H. –E. Lee and K. T. Nam, "Phase transformation from hydroxyapatite to the secondary bone mineral, whitlockite", *J. Mater. Chem. B*, 3, 1342, 2015.

5. H. L. Jang, K. Lee, C. S. Kang, H. K. Lee, H. Y. Ahn, H. Y. Jeong, S. Park, S. C. Kim, K. Jin, J. Park, T. Y. Yang, J. H. Kim, S. A. Shin, H. N. Han, K. H. Oh, H. Y. Lee, J. Lim, K. S. Hong, M. L. Snead, J. Xu and K. T. Nam, "Biofunctionalized Ceramic with Self-Assembled Networks of Nanochannels", *ACS nano*, 9, 4447, 2015.

6. E. Pallecchi, Z. Chen, G. E. Fernandes, Y. Wan, J. H. Kim and J. Xu, "A thermal diode and novel implementation in a phase-change material", *Mater. Horiz.*, 2, 125, 2015.

7. D. Oller, G. E. Fernandes, J. H. Kim, and J. Xu, "Investigation of quantum confinement within the tunneling-percolation transition for ultrathin bismuth films", *Physica B: Condens. Mat.*, 475, 117, 2015.

8. H. Q. Nguyen, S. M. Hollen, and J. M. Valles, Jr., J. Shainline, and J.M. Xu, "Disorder influences the quantum critical transport at a superconductor-to-insulator transition", *Phys. Rev. B*, 92, 140501(R) 2015.

9. P. Tae, C. Zhao, G. Fernandes, J. H. Kim, and J. Xu, "Molecular weight effects on the phasechange-enhanced temperature coefficient of resistance in carbon nanotube/poly(Nisopropylacrylamide) composites", *Nanotechnol.*, 26, 215705, 2015.

10. H. L. Jang, K. Jin, J. Lee, Y. Kim, S. H. Nahm, K. S. Hong, K. T. Nam, "Revisiting the Whitlockite, the Second Most Abundant Biomineral in Bone: Nanocrystal Synthesis in Physiologically Relevant Condition and Biocompatibility Evaluation" *ACS Nano*, 8, 634, 2014.

11. Y. Kim, S. A. Shin, J. Lee, K. D. Yang and K. T. Nam, "Hybrid system of semiconductor and photosynthetic protein", *Nanotechnol.*, 25, 342001, 2014.

12. D. -J. Lee, J. Kwon, J. Kim, K. -J. Kim, Y. -Ho. Cho, S. -Y. Cho, S. -H. Kim, J. Xu, and Ki. -B. Kim, "Ultrasmooth, High Electron Mobility Amorphous In-Zn-O Films Grown by Atomic Layer Deposition", *J. Phys. Chem. C*, 118, 408, 2014.

13. F. Wahab, G. E. Fernandes, S.W. Jung, J. H. Kim, K. -B. Kim and J. M. Xu, "High Seebeck coefficient in solution grown PbS films", *J. Electron. Mater.*, 43, 348, 2014.

14. Y. Park, Y. Hirose, S. Nakao, T. Fukumura, J. Xu, and T. Hasegawa, "Quantum confinement effect in Bi anti-dot thin films with tailored pore wall widths and thicknesses", *Appl. Phys. Lett.*, 104, 023106, 2014.

15. S. M. Hollen, J. Shanline, J. M. Xu, and J. M. Valles Jr. "Cooper Pair Insulator phase induced in amorphous Pb0.9Bi0.1 thin films", *Physica C*, 486, 23, 2013.

16. D. -J. Lee, J. -Y. Kwon, S. -H. Kim, K. -J. Kim, J. Xu, and K. -B. Kim, "Atomic layer deposition of Ti-doped ZnO films with enhanced electrical conductivity and mobility", *J. Mater. Chem. C*, 1, 4761, 2013.

17. G. E. Fernandes, D. -J. Lee, J. H. Kim, K.-B. Kim, and J. Xu, "Infrared and microwave shielding of transparent Al-doped ZnO superlattice grown via atomic layer deposition", *J. Mater. Sci.*, 48, 2536, 2013.

18. G. Fernandes, J. H. Kim, and J. M. Xu, "Thermoelectric response of carbon nanotube films to Au-nanoparticle incorporation", *Mater. Res. Bull.*, 48, 2950, 2013.

b) Papers published in peer-reviewed conference proceedings

1. J. H. Kim, H. L. Jang, K. T. Nam and J. Xu, "Concept, Theory, Design, and Experimental Tests of Self-Powered Lubrication in Ceramic Composite and Rotors", Applied Mechanics and Mechanical Engineering (AMME-16) (Invited), May 27-29, Cairo, Egypt, 2014..

2. Ki Tae Nam, Hae Lin Jang, Hye Kyoung Lee, Jaehun Lee, Younghye Kim and

Hyo-Yong Ahn. Revisiting Whitlockite, the second major inorganic components in bone tissue: Nanocrystal synthesis and evaluation as a cell scaffold, The Korean Ceramic Society, Korea, Apr 2014.

3. Ki Tae Nam, Hae Lin Jang, Kyoungsuk Jin, Jaehun Lee and Younghye Kim. Revisiting Whitlockite, One of the Major Inorganic Components in Bone Tissue: Nanocrystal Synthesis and Evaluation as a Cell Scaffold. Joint Symposium of Nature-inspired Technology (ISNIT), Japan, Feb 2014.

4. Ki Tae Nam, Hae Lin Jang, Jin Ho Kim, Hye Kyoung Lee, Hyo-Yong Ahn, Sunghak Park, Malcolm L. Snead and Jimmy Xu. Making bioceramic 'alive' by self-powered capillary supply of nutrients through built-in nanochannels. International Conference on Competitive Materials and Technology Processes (ic-cmtp3), Hungary, Oct. 2014.

c) Papers published in non-peer-reviewed journals and conference proceedings

d) Conference presentations without papers

Hae Lin Jang, Kyoungsuk Jin, Jaehun Lee, Younghye Kim and Ki Tae Nam. Synthesis of Whitlockite nanoparticles, the second most abundant biomineral in osseous tissue. *Materials Research Society*, Apr 2014

e) Manuscripts submitted but not yet published

1. D. Oller, D. He, J. H. Kim, D. Pacifici, J. Xu, and G. E. Fernandes, "Color gamuts arising from absorber-dielectric-metal optical resonators", Adv. Opt. Mater., Submitted.
2. J. H. Kim, H. L. Jang, K. T. Nam and J. Xu, "Facile fabrication of capillary-network enabled Hydroxyapatite composites for fluidic and lubricant delivery", Journal of Composite Materials, Submitted.

f) A list any interactions with industry or with Air Force Research Laboratory scientists or significant collaborations that resulted from this work.

f-1. Collaboration with industry

-There is an interaction between our team and Iljin materials, a Korean company, about development and commercialization of hydroxyl apatite bone cement.

-We submitted a proposal to Samsung Science & Technology Foundation, based on the same subject.

-Discussion with LG display is in progress in terms of industrializing these achievements.

-As a dividend of the research, a "Scalable Nano Manufacturing' project supported by Materion Ltd (HQ, near Brown University) and NSF was launched.

f-2. Research activity with ARFL

-Jae Hun Lee in Prof. Nam's group attended 9th International Symposium on Nature-Inspired Technology (ISNIT) to present our work, "Development of Peptide-based Dielectrics and Active Layers for Bio-organic Field Effect Transistor (BiOFETs)" on January 13, 2016.

-Ik Rang Choe in Prof. Nam's group attended 9th International Symposium on Nature-Inspired Technology (ISNIT) to present our work, "Water-floating giant sheets from helical peptide pentamers"on January 15, 2016. After presentation, we discussed commercialization of our achievements with staff in LG Display

-Yoonyoung Lee in Prof. Nam's group attended 2nd International Conference on Mechanics of Composites, July 11, 2016, and gave an oral presentation about our collaboration work, "Facile fabrication of capillary-network enabled self-powered fluidic supply in composites".

-A team of researchers from Korea, supported by AOARD, visited Brown University on May 17-18, 2016 and had a teleconference (via Skype) with Luke Bissell's group of Wright-Patterson AFRL.

Attachments: Publications a), b) and c) listed above if possible.